KONA Powder and Particle Journal

KONA Powder and Particle Journal No. 43 (2026) 249–268/https://doi.org/10.14356/kona.2026014 Original Research Paper

Exploring One-Dimensional Uniaxial Compression through a Granular Micromechanics Model†

Nurettin Yilmaz[1], Luca Placidi[2] and Anil Misra[1]*

[1] *Department of Civil and Environmental Engineering, Florida International University, USA*
[2] *Department of Engineering, Telematic University Pegaso, Italy*

Uniaxial or one-dimensional compression is widely used in granular material processing to produce granular compacts and is a key experimental method for evaluating the compressibility of granular materials. In this study, the granular micromechanics approach (GMA) was applied to simulate the one-dimensional uniaxial compression behavior of granular packing. GMA offers a continuum modeling paradigm that connects the macroscale response to the grain-scale mechanisms. To describe the stiffening behavior that elasto-frictional granular materials exhibit in confined compression, the elastic energy functional and dissipation potential were modified from previous versions of GMA-based models. The elastic energy of a grain pair was formulated to include a higher-order dependence on the normal relative displacement of the grain pair. The dissipation potential was also modified by incorporating coupling between plastic parameters that characterize plastic deformation accumulation as the grain-pair experiences compression and/or tension during loading process. The modified model, derived in the framework of geometrically nonlinear deformations, was then applied to replicate experimentally measured 1D compression behavior of granular materials undergoing large compression. The results reveal nearly universal scaling with respect to the model parameters for predicting the behavior of granular materials with different particle types or initial densities. A parametric study was conducted to determine the evolution of the microscale stored elastic energy and dissipation parameters in terms of grain-pair directions. In addition, this paper provides a brief literature review of experimental observations and modeling approaches related to powder compaction behavior.

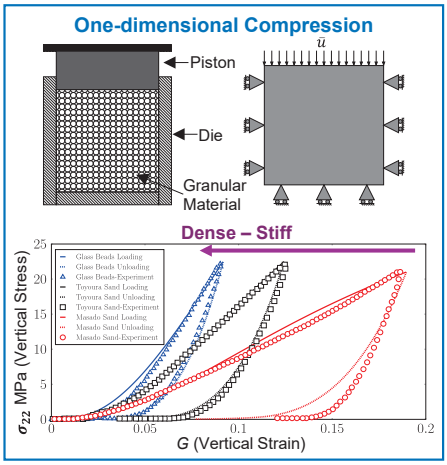

Keywords: one-dimensional compression, powder compaction, granular micromechanics, damage and plasticity mechanics, variational-based model

1. Introduction

A class of granular materials, commonly encountered as heaps of discrete particles or powders, has been extensively investigated across various industries for its unique flow, plastic deformation, and compaction behaviors. The mechanical behavior of such materials is the subject of intensive research spanning fields such as geotechnical engineering, pharmaceutical manufacturing, food processing, and civil infrastructure. The unique mechanical properties of such elasto-frictional granular materials depend on a myriad of factors, including their initial density state (or solid fraction), heterogeneity, loading history, particle surface characteristics, and interparticle interaction behavior. Among these factors, the behavior of this class of granular materials is strongly influenced by the elasto-frictional contact between grains. Such granular materials at relatively low solid fractions can exhibit fluid-like behavior under large macroscale shearing deformations, as discussed by Campbell (1990) and Goldhirsch (2003). Under such conditions, the elasto-frictional grain–grain contact may also involve inelastic collisional features. At higher solid fractions, such granular materials often exhibit compaction–dilation behavior under large macroscale shearing, leading to the so-called "critical state," in which grain-scale mechanisms—such as grain sliding, separation, and collapse/buckling of particle chains mediated by the elasto-frictional contacts—play a key role, as presented by Yilmaz et al. (2024, 2025).

Under highly confined conditions, one-dimensional compression becomes an important deformation mode in which the previously discussed grain-scale mechanisms also play an important role, depending on the initial density state or solid fraction. For this deformation condition, grain-scale mechanisms such as particle crushing, grain rearrangement, rotation/rolling, grain sliding, loss of lateral support, grain neighborhood densification, and strain localization give rise to complex mechanical behavior. For example, particle crushing in granular materials results in irreversible deformations, leading to a denser form through a reduction in initial void ratio. Interestingly, the so-called

† Received 12 February 2025; Accepted 28 April 2025
J-STAGE Advance published online 12 July 2025
* Corresponding author: Anil Misra;
Add: 10555 W Flagler Street, EC 3680. Miami, FL 33174, USA
E-mail: anmisra@fiu.edu
TEL: +1-305-348-3821

yield stress has been reported to increase due to crushing of granular material (see Yamamuro et al., 1996; Nakata et al., 2001, for investigations into the stress–initial void ratio relationship). Indeed, the macroscopic behavior of granular assemblies is expected to be elucidated through grain-pair interactions. In this paper, we discuss the compaction behavior of these materials under one-dimensional compression, assuming the grains to be cohesionless or weakly cohesive, such that the grain-scale behavior is dominantly elasto-frictional.

1.1 Review of powder compaction

Powder compaction is a manufacturing technique for crafting robust and high-performance products capable of withstanding a range of loading conditions, whose performance depends on the complex grain-scale interactions that evolve in granular materials under uniaxial compression. Powder compaction increases the mass density while maintaining constant mass and, in the process, rearranging and deforming grains, irrespective of the stiff or soft interface properties. The packed microstructures emerge from densifying loose powders into solid entities, thereby acquiring the desired mechanical behavior of granular materials through compression, causing volume reduction and consolidation of interparticle contact bonds. Compaction increases the stiffness, shear strength, and fragmentation strength of the resultant grain pack. Powder compaction has been extensively used to fabricate a wide variety of products including pharmaceutical pills (Wu et al., 2005, 2008) and other selected works (Leuenberger and Rohera, 1986; Mohan, 2012) for investigation of pharmaceutical tablet compaction), metallurgy manufacturing (Chtourou et al., 2002a, b; Sethi et al., 2008), and ceramic green microstructures (Vogler et al., 2007). In particular, die compaction represents the compression of powdered materials to obtain dense and uniform structures, i.e., maximum compression pressure or minimum form separation, by placing powders under defined boundary conditions in a die. To better understand the compaction process of ceramic powder, Niesz (1996) reviewed pertinent factors and their associations with green microstructure. Notably, the cohesive frictional behavior plays a key role in the fracture mechanism during powder compaction within a die (see, for instance, Tahir and Ariffin, 2006). Bandara et al. (2021) performed mechanical testing on proppant packs in oil/gas recovery processes and revealed significant plastic deformation during the first loading cycle. Lunar and Martian regolith compaction behavior has also been experimentally explored using powder simulants with similar compositions to the regolith on the Moon and Mars (Grindrod et al., 2010; Suescun-Florez et al., 2015). In addition, the mechanical behavior of a range of granular materials has been examined based on experimental investigations, such as those of clayey sands and fine-grained soils (Monkul and Ozden, 2007; Xu et al., 2009) and tailing dam material (Carrera et al., 2011).

1.2 Review of compaction behavior modeling

Numerical analysis of powder compaction has been explored using continuum finite element models (FEM) or discrete element models (DEM) or through coupled FEM-DEM approaches, as exemplified in the following works of Ransing et al. (2000); Sinka (2007); Güner et al. (2015). Several studies have explored the macroscopic response of one-dimensional compression of granular mechanics grounded in continuum mechanics. The macroscale behavior typically considers elastic and dissipative phenomena resulting from the development of grain-scale deformation. Along these lines, Roscoe and Burland (1968) used the modified Cam-clay model to predict the stress–strain behavior under compaction. Similarly, modifications to classical elasto-plastic theory have been used to model compaction, including the effects of grain breakage (see Pastor et al., 1990; Daouadji et al., 2001). Further, based on phenomenological considerations, Chong and Santamarina (2016) proposed a soil compressibility model to satisfy asymptotic void ratios by modifying existing models and functions at both low and high effective stress levels. Cocks (2001), Cocks and Sinka (2007) constructed constitutive models of plastically deforming powder compaction (metal), sintering (ceramic), and flow processes by offering valuable insights into the evolution of actual yield surfaces. Alternatively, Russell (2011) proposed that energy dissipation involves plastic work due to the creation of the surface area of the fragments and load distribution, and adapted this mechanism into a Cam-clay-type energy equation. Park et al. (1999) proposed a yield criterion by modeling metal powder die compaction which facilitates handling of bulk materials. Following a thermomechanical framework, Einav (2007a; b) introduced continuum breakage mechanics to model crushable granular materials in a series of articles in which the contribution of breakage (resulting in evolution of grain size distribution) and other dissipative mechanisms to the overall inelastic behavior of granular materials have been described (see the dissipative process modeling without plasticity in Part 1 (Einav, 2007a) and including plasticity in Part 2 (Einav, 2007b)). Many other models of powder compaction using the continuum approach have been considered (see, for example, Michrafy et al., 2002). In an alternate approach, Richard et al. (2005) considered statistical mechanics approaches to describe the dynamics of powder compaction and their seeming correspondence with glass formers.

In contrast to continuum FEM models, DEM directly considers grain-scale properties, such as stiffness, strength, shapes, and sizes, and can be used to investigate one-dimensional compression with the ability to monitor the microscale behavior, including particle position and

contact force, and local packing density. At the same time, it can provide the evolution of macroscopic properties such as bulk density and shear strength. DEM can clearly encompass many types of heterogeneous granular systems; however, the challenge is that while observing the contact interactions, displacement fields, and forces of individual grains, the computational cost increases inordinately as a range of complexity is desired to be modeled. The key drawback of DEM is not only computational time but also the accuracy and suitability of the simulation algorithms, and more importantly, the complexity of developing detailed realistic models of grain-contact behavior, the simulation result interpretation, and their dependence upon the domain size. DEM has been used to study certain features of the compaction behavior of idealized granular systems. For example, Cheng et al. (2003) employed DEM to investigate the characteristics of crushable sands, using tri-axial tests to validate the numerical simulations and comparing the simulation results with experiments conducted on silica sand. Minh and Cheng (2013) presented the effect of particle-size distribution on the one-dimensional compression of granular packing with nondeformable particles and compared the outcome with experimental data. Several DEM simulations have been performed for crushable particles (see Harireche and McDowell, 2003; Cil and Alshibli, 2012 for the effect of particle fracture and plastic deformation). Bolton et al. (2008) investigated the mechanical behavior of irregularly packed agglomerates by comparing breakable and unbreakable assemblies. Using a fractal distribution of particles, McDowell and de Bono (2013) simulated one-dimensional compression and explored the particle-crushing mechanism and fractal particle-size distribution, replacing the broken particles with new smaller particles while preserving mass. To investigate the cyclic loading phenomena for grain packs, García and Medina (2006) used a numerical simulation based on DEM, which showed decreased dissipation in a dense case. Wiącek et al. (2017) investigated the evolution of contact force in binary granular mixtures under uniaxial compressive load using 3D DEM simulations; however, other grain-scale measures, such as the directional evolution of either the dissipation and elastic energy or the contact force, were characteristically overlooked. Discrete description (see selected works that also include a brief review on the micromechanics grain breakage under one-dimensional compression, e.g., Jiang et al., 2014; Zhou et al., 2014; de Bono and McDowell, 2014; Cil and Alshibli, 2014; Hanley et al., 2015; Wu et al., 2022) or hybrid approaches blending discrete and continuum methodologies have also been developed (such as the combined couplings explored in Onate and Rojek, 2004; Villard et al., 2009; Chung et al., 2016). Finally, Ransing et al. (2000) considered compression of powders consisting of ductile and brittle particles using DEM and compared the results with those from continuum approaches.

More significantly, methods for the continuum modeling of granular materials in terms of grain-scale mechanisms by referring to the orientational distribution of contacts have been proposed (Jagota et al., 1988; Chang and Misra, 1989). Following this modeling direction, Chang and Hicher (2005) established an elastic-plastic model by following Hertz-Mindlin's elastic law and Mohr-Coulomb's plastic law to derive the stress–strain relationship for compaction. More recently, the authors have advanced a granular micromechanics approach (GMA) for continuum modeling that considers Piola's ansatz for micro-macro kinematic identification (Misra et al., 2021) and grain-pair elastic-damage-plastic interactions to find the elastic energy density and dissipation potential at the macroscale (Placidi et al., 2021; Yilmaz et al., 2024, 2025).

1.3 Present work

During one-dimensional compression of elasto-frictional granular materials, a stiffer assembly is created while accruing irrecoverable deformations. While compaction leads to a transition from a loose to dense state, the mechanical energy required for the transition is influenced by the grain-pair contacts. The core thrust of this work is to address the concept of one-dimensional compression by exploiting grain-scale mechanisms. These mechanisms are activated using the framework of elastic and dissipation energy functionals in GMA-based continuum mechanics. The energy terms are developed from the damage-elasto-plastic springs, which represent effective grain-pair interactions in both the normal and tangential directions. The resultant continuum theory was applied to investigate the macroscopic behavior during the loading–unloading cycle of one-dimensional compression. Since such compression experiments are analyzed as a single continuum material point in terms of strain and the measured reaction is interpreted as stress, the simulation here assumes homogeneous deformations. The results highlight the elastic hardening behavior and the evolution of damage and plasticity, which are crucial factors affecting the behavior of granular materials.

This paper is organized as follows. In **Section 2**, we report a GMA, including a new type of elastic and dissipation energy terms based on a generic grain-pair interaction and a hemi-variational method to derive Karush-Kuhn-Tucker (KKT)-type conditions for irreversible phenomena. In **Section 3**, we present the numerical investigations by replicating experimental observations in one-dimensional compression. In **Section 4**, the key findings are summarized, and future research directions are discussed.

2. Granular micromechanics approach

Continuum modeling remains the most feasible approach for describing the mechanical behavior of complex

materials in which the stress–strain response exhibits non-standard behavior that could be dependent upon the sequence of loading or loading paths. To this end, variational and energy-based methods, which trace their origins to the earliest efforts at describing mechanical systems, have proven to offer particularly robust solutions (dell'Isola and Misra, 2023). In this regard, significant attempts have been made at deriving models for solids of complex microstructures undergoing damage and other loading-induced internal transformations using energy- and variational methods as a basis (see, for example, Placidi, 2016; Fabbrocino and Carpentieri, 2017; Mancusi et al., 2017; dell'Isola et al., 2020). These methods have been harnessed to develop models beyond classical elasticity theory to accurately predict the behavior of complex multi-scale structures (see, for example, strain gradient theory (Eremeyev et al., 2021; Aydin et al., 2022; Sarar et al., 2023)). These advanced higher-gradient theories (Abali et al., 2017, 2019; Yang et al., 2020) generalize classical continuum theories to elucidate geometric and size-dependent effects and incorporate geometrical nonlinearity (Abali et al., 2015; Fedele, 2022a, b; dell'Isola et al., 2022; Fedele et al., 2024). These novel mathematical models have found application for a range of materials, including pantographic metamaterial (Eremeyev et al., 2018; Stilz et al., 2022; Yildizdag et al., 2023), metamaterial of granular motif (Giorgio et al., 2022), bone remodeling (Giorgio et al., 2023), and masonry (Ramaglia et al., 2018; Grande et al., 2020; Reccia and Eremeyev, 2024).

From the viewpoint of granular materials, continuum models to investigate complex assemblies consisting of many particles require a detailed understanding of the grain-scale phenomena and how they are connected to the macroscale response. Recent applications have shown that the GMA provides a framework for bridging the grain and macroscale behaviors for a variety of granular material phenomena, including its elasticity (Barchiesi et al., 2021), damage (Timofeev et al., 2021), and coupled damage and plasticity (Placidi et al., 2021; Yilmaz et al., 2024, 2025). For instance, Placidi et al. (2024) demonstrated the capability of GMA by replicating the experimental results for ultrahigh-performance fiber-reinforced concrete (UHP-FRC). For a completely different granular system in which the grains interact primarily with frictional contacts, Yilmaz et al. (2024) investigated the emergence of critical states by applying a GMA with appropriately formulated effective grain-scale elastic and dissipation energy functionals. The present work aims at the so-called one-dimensional compression of granular packing, accounting for grain-scale phenomena, by using GMA. For this purpose, new types of elastic energy and dissipation energy potentials are integrated into the constitutive model for effective grain-pair interactions. As in our previous works dealing with dissipative granular systems, a hemi-variational approach was used to obtain new evolution equations for damage and plastic deformation in the form of the Karush-Kuhn-Tucker (KKT)-type conditions to predict these irreversible quantities at the grain-scale. We then demonstrate the new model's capability for replicating the compaction behavior of elasto-frictional granular materials under one-dimensional compression. The remainder of this section briefly describes the main aspects of the GMA-based mathematical model.

2.1 Piola's ansatz and continuum deformation measurements

A discrete description of a granular system focuses on a set of N grains located in a 2D Euclidean space E^2. While each i^{th} grain's position in the reference configuration is represented by $\mathbf{X}_i$, its location in the actual configuration at time t is determined by the placement function $\boldsymbol{\chi}_i(t)$ as outlined below:

$$\mathbf{x}_i = \boldsymbol{\chi}_i(t) = \mathbf{X}_i + \mathbf{u}_i(t), \quad i = 1, \ldots, N, \tag{1}$$

where $\mathbf{u}_i(t)$ represents the displacement vector for the i^{th} grain. For the continuum description, we consider a continuous body $\mathcal{B}$ within E^2 comprising an infinite number of grains. The position of each material point within $\mathcal{B}$ is designated by $\mathbf{X}$ in the reference configuration, while its position in the actual configuration at time t is determined by the placement function $\boldsymbol{\chi}(\mathbf{X}, t)$ as follows:

$$\mathbf{x} = \boldsymbol{\chi}(\mathbf{X}, t) = \mathbf{X} + \mathbf{u}(\mathbf{X}, t) \tag{2}$$

where the displacement vector is symbolized by $\mathbf{u}(\mathbf{X}, t)$. Piola's ansatz establishes the relationship between both descriptions, as developed by dell'Isola et al. (2015) as follows:

$$\boldsymbol{\chi}(\mathbf{X}_i, t) = \boldsymbol{\chi}_i(t), \quad i = 1, 2, \ldots, N \tag{3}$$

Piola's ansatz determines the correspondence between the placements $\boldsymbol{\chi}_i$ for the discrete description containing N grains and the placement $\boldsymbol{\chi}$ for the continuous body within $\mathcal{B}$.

When the two adjoined representative grains n and p in the reference configuration are positioned at $\mathbf{X}_n$ and $\mathbf{X}_p$, the vector defining the relative position in the reference configuration by adjusting the position of grain n relative to grain p is given by

$$\mathbf{X}_n - \mathbf{X}_p = L\,\hat{\mathbf{c}} \tag{4}$$

Here, $\hat{\mathbf{c}}$ represents a unit vector originating from grain p toward grain n, while L represents the distance between these two representative grains. As a consequence, the grain-pair distance L depends neither on the sizes of particular grains of the discrete model nor on the orientation $\hat{\mathbf{c}}$ of the continuum model. Thanks to Piola's ansatz, $\mathbf{x}_n = \boldsymbol{\chi}(\mathbf{X}_n, t)$ and $\mathbf{x}_p = \boldsymbol{\chi}(\mathbf{X}_p, t)$ give the positions of the grains in the actual configuration. Consequently, the following

expression gives the vector indicating the relative position in the actual configuration

$$\mathbf{x}_n - \mathbf{x}_p = \boldsymbol{\chi}(\mathbf{X}_n, t) - \boldsymbol{\chi}(\mathbf{X}_p, t) \tag{5}$$

Based on the prior works of Placidi et al. (2021; 2022a; b), the objective relative displacement $\mathbf{u}^{np}$ is defined as follows:

$$\mathbf{u}^{np} = \mathbf{F}^T(\mathbf{x}_n - \mathbf{x}_p) - (\mathbf{X}_n - \mathbf{X}_p) \tag{6}$$

where $\mathbf{F}$ is the deformation gradient ($\mathbf{F} = \nabla\boldsymbol{\chi}$). Considering an identical deformation level for the grains, the Taylor series expansion of the placement $\boldsymbol{\chi}(\mathbf{X}_n, t)$ around $\mathbf{X} = \mathbf{X}_p$ yields

$$\mathbf{x}_n = \boldsymbol{\chi}(\mathbf{X}_n, t) \cong \mathbf{X}_p + L\,\mathbf{F}\,\hat{\mathbf{c}} \tag{7}$$

where

$$\mathbf{F} = \nabla\boldsymbol{\chi}\big|_{\mathbf{X}=\mathbf{X}_p} \tag{8}$$

Unless otherwise stated, index notation will be used for clarity in the remaining parts of this work. Consequently, the objective relative displacement:

$$u_i^{np} = 2LG_{ij}\hat{c}_j \tag{9}$$

where $\boldsymbol{G}$ is the Green–St-Venant tensor expressed as

$$G_{ij} = \frac{1}{2}(F_{ai}F_{aj} - \delta_{ij}) \tag{10}$$

The projection of the objective relative displacement vector onto the unit vector $\hat{\mathbf{c}}$, scaled by half, generates the normal displacement (a scalar quantity) as follows:

$$u_\eta = \frac{1}{2}u_i^{np}\hat{c}_i \tag{11}$$

then the projection of the objective relative displacement onto the unit vector orthogonal to $\hat{\mathbf{c}}$ is identified as the tangent displacement vector as follows:

$$u_{\tau_i} = u_i^{np} - u_j^{np}\hat{c}_j\hat{c}_i \tag{12}$$

By simply replacing **Eqn. (9)** into **Eqns. (11)** and **(12)**, respectively, returns the following equations for the normal displacement, its square, and the square of the norm of the tangent displacement vector:

$$u_\eta = LG_{ij}\hat{c}_i\hat{c}_j \tag{13}$$

$$(u_\eta)^2 = L^2G_{ij}G_{ab}\hat{c}_i\hat{c}_j\hat{c}_a\hat{c}_b \tag{14}$$

$$(u_\tau)^2 = 4L^2G_{ij}G_{ab}(\delta_{ia}\hat{c}_j\hat{c}_b - \hat{c}_i\hat{c}_j\hat{c}_a\hat{c}_b) \tag{15}$$

where $u_\tau = \sqrt{u_{\tau_i}u_{\tau_i}}$. It is worth mentioning that this study only investigated homogeneous deformation. Thus, the gradient of the Green–St-Venant tensor does not arise in **Eqns. (13)–(15)** ($G_{ij,h} = 0$). Under a general loading condition, Uin which non-homogeneous deformation may be expected (such as Placidi et al., 2024), the strain gradient components are required and, therefore, are included here to present complete theoretical ideas. The normal u_η and the squared tangential u_τ^2 displacements are partitioned into elastic and plastic components as follows:

$$u_\eta = u_\eta^{el} + u_\eta^{pl}, \quad u_\tau^2 = u_\tau^{el,2} + u_\tau^{pl,2} \tag{16}$$

Additionally, λ_η^t and λ_η^c serve the tension and compression plastic variables, respectively. The difference between the two plastic variables specifies the plastic normal displacement as follows:

$$u_\eta^{pl} = \lambda_\eta^t - \lambda_\eta^c \tag{17}$$

The following expression gives the quadratic and quartic powers of the elastic normal displacement

$$\begin{aligned}(u_\eta^{el})^2 &= (u_\eta - u_\eta^{pl})^2 \\ &= L^2G_{ij}G_{ab}\hat{c}_i\hat{c}_j\hat{c}_a\hat{c}_b - 2Lu_\eta^{pl}G_{ij}\hat{c}_i\hat{c}_j + (u_\eta^{pl})^2\end{aligned} \tag{18}$$

and

$$\begin{aligned}(u_\eta^{el})^4 = (u_\eta - u_\eta^{pl})^4 &= L^4G_{ij}G_{ab}G_{cd}G_{ef}\hat{c}_i\hat{c}_j\hat{c}_a\hat{c}_b\hat{c}_c\hat{c}_d\hat{c}_e\hat{c}_f \\ &- 4L^3G_{ij}G_{ab}G_{cd}\hat{c}_i\hat{c}_j\hat{c}_a\hat{c}_b\hat{c}_c\hat{c}_d(u_\eta^{pl}) + 6L^2G_{ij}G_{ab}\hat{c}_i\hat{c}_j\hat{c}_a\hat{c}_b(u_\eta^{pl})^2 \\ &- 4LG_{ij}\hat{c}_i\hat{c}_j(u_\eta^{pl})^3 + (u_\eta^{pl})^4\end{aligned} \tag{19}$$

2.2 Elastic energy

Let U^{np} denote the total elastic energy associated with the effective grain-pair interaction between two contacting grains, n and p, for whom the line connecting their centroids is aligned in the direction $\hat{\mathbf{c}}$. We postulate that U^{np} can be expressed as follows in terms of the normal and tangential decomposition of the objective total relative displacement between the grains (**Eqns. (18)** and **(19)**).

$$U^{np} = \frac{1}{2}k_{\eta D}(u_\eta^{el})^2 + \frac{1}{4}k_{\eta\eta D}(u_\eta^{el})^4 + \frac{1}{2}k_{\tau D}(u_\tau^{el})^2 \tag{20}$$

In **Eqn. (20)**, $k_{\eta D}$ symbolizes the damaged normal stiffness (different in tension and in compression) while $k_{\eta\eta D}$ indicates the damaged duffing stiffness:

$$\begin{aligned}k_{\eta D} &= \tilde{k}_{\eta D}(u_\eta^{el}) \\ &= \frac{1}{2}(k_{\eta D}^t + k_{\eta D}^c) + \frac{1}{\pi}(k_{\eta D}^t - k_{\eta D}^c)\arctan\left(\frac{u_\eta^{el}}{\alpha}\right)\end{aligned} \tag{21}$$

$$k_{\eta\eta D} = \frac{k_{nn}k_{\eta D}}{L^2} \tag{22}$$

where, in **Eqn. (21)**, α is a parameter regularizing the tension–compression transition, and k_{nn} is a non-dimensional material constant indicating the weight of the new duffing contribution. The grain-scale normal stiffness asymmetry under tension and compression was inspired by the work of Misra and Yang (2010) on cohesive materials modeled via

pseudo-bonds. The first and third terms in **Eqn. (20)** are the standard ones that are minimally needed to describe linear elastic behavior as discussed by Barchiesi et al. (2021); Placidi et al. (2021); Timofeev et al. (2021); Placidi et al. (2022a, b, 2024); Yilmaz et al. (2024, 2025). The second term in **Eqn. (20)** is quartic with respect to the elastic normal displacement u_η^{el}, and has been introduced in this work to account for the grain-pair stiffening effect under compression. Therefore, the behavior corresponds not anymore to a linear standard spring but to a cubic (duffing) non-standard spring. The reason for such a new term is connected to the necessity of including the nonlinear stiffening that contacting grain pairs with rough surfaces experience under compression (see Misra and Marangos, 2011; Misra and Huang, 2012), which is a significant feature of the uniaxial compression tests we aim to model in this paper.

Two damage variables reduce the damaged tension $k_{\eta\mathrm{D}}^{\mathrm{t}}$ and compression $k_{\eta\mathrm{D}}^{\mathrm{c}}$ normal stiffness, and the damaged tangent $k_{\tau\mathrm{D}}$ stiffness, as given by

$$\begin{aligned} k_{\eta\mathrm{D}}^{\mathrm{t}} &= k_\eta^{\mathrm{t}}\left(1-D_\eta\right) \\ k_{\eta\mathrm{D}}^{\mathrm{c}} &= k_\eta^{\mathrm{c}}\left(1-D_\eta\right) \\ k_{\tau\mathrm{D}} &= k_\tau\left(1-D_\tau\right) \end{aligned} \tag{23}$$

where, k_η^{t} and k_η^{c} refer to the non-damaged normal stiffness in tension and compression, respectively, and k_τ denotes the non-damaged tangential stiffness. The sign of u_η^{el} determines whether the current direction $\hat{\mathbf{c}}$(or *np* pair) is characterized by tension or compression. As illustrated in **Fig. 1**, it is evident that $k_\eta^{\mathrm{t}} \ll k_\eta^{\mathrm{c}}$. As α approaches zero, an abrupt transition between tension and compression is achieved based on the properties of the Heaviside function. Note that the value of α should be much smaller than u_η^{el}. The normal D_η and the tangential D_τ damage variables characterize the damage phenomenon. The damaged stiffness (and the corresponding elastic energy described in **Eqn. (20)**) approaches zero when the damage quantities approach the unity values.

Let us consider that within a specimen composed of frictional granular material, there are possible M grain-pair

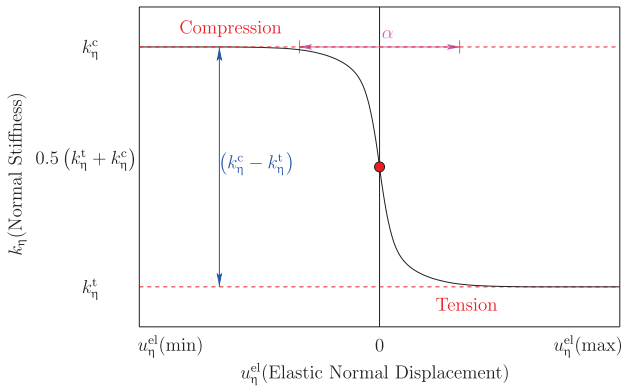

Fig. 1 Normal stiffness k_η under tension and compression as a function of elastic normal displacement u_η^{el}.

interactions. The total elastic energy is obtained by summing the elastic energy U^{np} over all such pairs as expressed below

$$U_M = \sum_{np=1}^{M} U^{np} \tag{24}$$

In line with the simple homogenization rule (see selected works that also include a brief review about the details of the adapted homogenization approach (Barchiesi et al., 2021; Misra et al., 2021), an elastic energy density is assumed with respect to the definition of the continuum as follows:

$$\begin{aligned} &U_M \underset{M\to\infty}{\to} U \\ &= \int_{\mathcal{S}} \left[\frac{1}{2}k_{\eta\mathrm{D}}\left(u_\eta^{\mathrm{el}}\right)^2 + \frac{1}{4}k_{\eta\eta\mathrm{D}}\left(u_\eta^{\mathrm{el}}\right)^4 + \frac{1}{2}k_{\tau\mathrm{D}}\left(u_\tau^{\mathrm{el}}\right)^2\right]\mathrm{d}l \end{aligned} \tag{25}$$

where all grain pairs are identified by their direction $\hat{\mathbf{c}}$. The region S is the unit circle containing $\hat{\mathbf{c}}$, and dl represents the infinitesimal element dθ, as elaborated by Placidi et al. (2022b). Within an orthonormal frame of reference (O, $\hat{\mathbf{e}}_1$, $\hat{\mathbf{e}}_2$), the orientation $\theta \in [0,2\pi]$ identifies the unit vector, $\hat{\mathbf{c}} = \cos\theta\hat{\mathbf{e}}_1 + \sin\theta\hat{\mathbf{e}}_2$, using polar coordinates. The stiffness and damage parameters depend on the orientation in the continuum description: $k_\eta = \tilde{k}_\eta(\theta)$, $k_{\eta\eta} = \tilde{k}_{\eta\eta}(\theta)$, $k_\tau = \tilde{k}_\tau(\theta)$, $D_\eta = \tilde{D}_\eta(\theta)$ and $D_\tau = \tilde{D}_\tau(\theta)$.

The continuum elastic energy density can be expressed using **Eqns. (13)–(19)** as follows:

$$\begin{aligned} U = &\frac{1}{2}\mathbb{C}_{ijab}G_{ij}G_{ab} + \frac{1}{3}\mathbb{L}_{ijabcd}G_{ij}G_{ab}G_{cd} \\ &+ \frac{1}{4}\mathbb{N}_{ijabcdef}G_{ij}G_{ab}G_{cd}G_{ef} + \mathbb{P}_{ij}G_{ij} \end{aligned} \tag{26}$$

where $\mathbb{C}_{ijab}$ (4^{th} – order), $\mathbb{L}_{ijabcd}$ (6^{th} – order), $\mathbb{N}_{ijabcdef}$ (8^{th} – order) and $\mathbb{P}_{ij}$ (2^{nd} – order) are elastic stiffness tensors. These tensors are defined as follows:

$$\begin{aligned} \mathbb{C}_{ijab} = &L^2\int_{\mathcal{S}} k_\eta\left(1-D_\eta\right)\hat{c}_i\hat{c}_j\hat{c}_a\hat{c}_b\,\mathrm{d}l \\ &+ L^2\int_{\mathcal{S}} 3k_{\eta\eta}\left(1-D_\eta\right)\hat{c}_i\hat{c}_j\hat{c}_a\hat{c}_b\left(u_\eta^{\mathrm{pl}}\right)^2\mathrm{d}l \\ &+ L^2\int_{\mathcal{S}} k_\tau\left(1-D_\tau\right)\left(\left(\delta_{ia}\hat{c}_j\hat{c}_b + \delta_{ib}\hat{c}_j\hat{c}_a + \delta_{ja}\hat{c}_i\hat{c}_b\right.\right. \\ &\left.\left. + \delta_{jb}\hat{c}_i\hat{c}_a\right) - 4\hat{c}_i\hat{c}_j\hat{c}_a\hat{c}_b\right)\mathrm{d}l \end{aligned} \tag{27}$$

$$\mathbb{L}_{ijabcd} = -L^3\int_{\mathcal{S}} 3k_{\eta\eta}\left(1-D_\eta\right)\hat{c}_i\hat{c}_j\hat{c}_a\hat{c}_b\hat{c}_c\hat{c}_d\left(u_\eta^{\mathrm{pl}}\right)\mathrm{d}l \tag{28}$$

$$\mathbb{N}_{ijabcdef} = L^4\int_{\mathcal{S}} k_{\eta\eta}\left(1-D_\eta\right)\hat{c}_i\hat{c}_j\hat{c}_a\hat{c}_b\hat{c}_c\hat{c}_d\hat{c}_e\hat{c}_f\,\mathrm{d}l \tag{29}$$

$$\begin{aligned} \mathbb{P}_{ij} = &-L\int_{\mathcal{S}} k_\eta\left(1-D_\eta\right)\hat{c}_i\hat{c}_j\left(u_\eta^{\mathrm{pl}}\right)\mathrm{d}l \\ &- L\int_{\mathcal{S}} k_{\eta\eta}\left(1-D_\eta\right)\hat{c}_i\hat{c}_j\left(u_\eta^{\mathrm{pl}}\right)^3\mathrm{d}l \end{aligned} \tag{30}$$

$\mathbb{C}_{ijab}$, $\mathbb{L}_{ijabcd}$, $\mathbb{N}_{ijabcdef}$, and $\mathbb{P}_{ij}$ comprise different powers of the normal elastic relative displacement u_η^{el}. These stiffness tensors are obtained by integrating all the considered

orientations using the trapezoidal rule. Because the quantity $\mathbb{P}_{ij}$ is a function of plastic deformation and contributes to the deformation energy density as a linear function of strain, we choose to include it in the list of stiffness values. Unlike previous studies by Placidi et al. (2021; 2022a; b), the effects of the normal plastic relative displacement u_η^{el} are seen both in $\mathbb{P}_{ij}$, also referred to as pre-stress tensor, and in other higher-order stiffness tensors. In addition, the duffing stiffness $k_{\eta\eta}$ injects the nonlinear effects in all other elastic stiffness tensors. Finally, in **Eqns. (27)–(30)**, the increase in damage results in a loss of stiffness. This loss can be explained as a decrease not only in the buckling and crumbling of chains and clusters due to normal damage but also in the side support and enclosure of these structures within grain neighborhoods from tangent damage.

2.3 Dissipation energy potential

We employed six fundamental scalar kinematic variables (one vectorial and five scalar variables) to determine the dissipation energy considering a generic grain pair: u_η and u_τ^2 (normal and squared tangential displacements), as well as D_η, D_τ, λ_η^t, and λ_η^c (describing damage and plasticity). The total dissipation energy potential W can be divided into damaged and plastic parts as follows:

$$W = W_D + W_{pl} \tag{31}$$

where W_D represents dissipated energy potential due to damage while W_{pl} represents dissipated energy potential due to plastic behavior. The term W_D can be further decomposed into its normal and tangential parts as follows:

$$W_D = W_D^\eta + W_D^\tau \tag{32}$$

where

$$W_D^\eta = \frac{1}{2}k_\eta (B_\eta)^2\left[-D_\eta + \frac{2}{\pi}\tan\left(\frac{\pi}{2}D_\eta\right)\right] \tag{33}$$

and

$$W_D^\tau = \frac{1}{2}k_\tau (B_\tau)^2 \left[2 + (D_\tau - 1)\left(2 - 2\log(1-D_\tau) + (\log(1-D_\tau))^2\right)\right] \tag{34}$$

In addition, B_η and B_τ are the characteristic displacements associated with the normal and tangent damage variables, respectively, which are expressed as follows:

$$B_\eta = \tilde{B}_\eta\left(u_\eta^{el}\right) = \frac{1}{2}\left(B_\eta^t + B_\eta^c\right) + \frac{1}{\pi}\left(B_\eta^t - B_\eta^c\right)\arctan\left(\frac{u_\eta^{el}}{\alpha}\right) \tag{35}$$

$$B_\tau = \tilde{B}_\tau\left(u_\eta^{el}\right) = \frac{1}{2}\left(B_{\tau_0} + \alpha_1 B_{\tau_0}\right) + \frac{1}{\pi}\left(B_{\tau_0} - \alpha_1 B_{\tau_0}\right)\arctan\left(\frac{u_\eta^{el}}{\alpha}\right) \tag{36}$$

here, α_1 introduces an additional constitutive parameter and regularizes the amount of characteristic damage displacements during tension. As explained for k_η in **Fig. 1**, the distinction is established between the tension and compression states in terms of the elastic relative displacement for the characteristic damage displacements B_η and B_τ. This process, where α approaches zero, was clarified in the previous **Subsection 2.2**, using the same properties of the Heaviside function. B_η^c and B_η^t, which are characteristic normal damage displacements in compression and tension, respectively, characterize normal damage dissipation, with $B_\eta^t \ll B_\eta^c$ relation assumed for lightly cohesive granular materials. Because of this correlation, normal damage reaches its limit faster in tension at very small elastic relative displacement. The characteristic tangent damage displacement B_{τ_0} explicitly governs B_τ with the interpretation of parameters α and α_1.

W_{pl} denotes the dissipated energy potential due to plastic behavior and is expressed as

$$W_{pl} = (1-D_\eta)^2\left(\sigma_\eta^t\lambda_\eta^t + \sigma_\eta^c\lambda_\eta^c + \sigma_{\eta\eta}^t(\lambda_\eta^t)^2 + \sigma_{\eta\eta}^c(\lambda_\eta^c)^2 + \sigma_{\eta\eta}^{tc}\lambda_\eta^t\lambda_\eta^c\right) \tag{37}$$

where the plasticity yielding conditions are governed for the coupled damage-elasto-plastic behavior under tension and compression by the constitutive parameters σ_η^t and σ_η^c, respectively. The parameters $\sigma_{\eta\eta}^t$ and $\sigma_{\eta\eta}^c$ characterize the plastic softening/hardening behavior under tension and compression, and $\sigma_{\eta\eta}^{tc}$ introduces the coupling between the evolution of the two plastic deformations. It is remarkable that the plastic dissipation energy density W_{pl} differs from that of previous works (Placidi et al., 2021; Timofeev et al., 2021), and the coupling term is added for the first time in the dissipated energy potential. In **Subsection 2.4**, the relevance and effects of these constitutive parameters indicated in the dissipation energy potential during one-dimensional compression are discussed about irreversible quantities.

2.4 Hemi-variational formulation: governing equations and Karush-Kuhn-Tucker conditions

Let us define $\mathcal{E}$ as the action functional of the system without considering the kinetic energy as follows:

$$\mathcal{E} = \int_{t_0}^{t_F}\left\{\int_{\mathcal{B}}(U+W)\,d\Omega - U^{ext}\right\}dt \tag{38}$$

where a monotonously increasing time sequence is described with $t_i \in \{t_i\}_{i=0,\ldots,F}$ in which $t_i \in \mathbb{R}$ and $F \in \mathbb{N}$. In addition, the external energy U^{ext} is presented via the following expression:

$$U^{ext} = \int_{\mathcal{B}}\mathbf{b}^{ext}\cdot\mathbf{u}\,d\Omega + \int_{\partial_t\mathcal{B}}\mathbf{t}^{ext}\cdot\mathbf{u}\,dl \tag{39}$$

here, $\mathbf{b}^{ext}$ specifies the distributed external force on the domain $\mathcal{B}$, and $\mathbf{t}^{ext}$ is the other external force distributed over

the boundary $\partial_{\mathbf{t}}\mathcal{B}$ of the boundary $\partial\mathcal{B}$, where Neumann boundary conditions are employed.

Here, we denote displacement array $\mathbf{u}(\mathbf{X}, t_i)$ for each time $t = t_0, t_1, \ldots, t_M$. This series AM_t gives kinematically admissible displacements for a specific time t, and the group AV_t is the set of kinematically admissible variations such that $\delta\mathbf{u}(\mathbf{X}, t_i) \in AV_t$. For instance, the imposed Dirichlet boundary conditions on a part of the boundary, also designated as $\partial_{\mathbf{u}}\mathcal{B}$, constrain the kinematically admissible displacement. Thus, the overall boundary $\partial\mathcal{B}$ is divided into two parts as $\partial_{\mathbf{u}}\mathcal{B}$ for displacements and $\partial_{\mathbf{t}}\mathcal{B}$ for Neumann (traction) conditions, such that $\partial\mathcal{B} = \partial_{\mathbf{u}}\mathcal{B} \cup \partial_{\mathbf{t}}\mathcal{B}$,

$$\mathbf{u} = \bar{\mathbf{u}} \quad \forall \mathbf{X} \in \partial_{\mathbf{u}}\mathcal{B} \tag{40}$$

Damage and plasticity are considered irreversible kinematic quantities; thus, their admissible variation can only be positive as

$$\left(\delta D_\eta, \delta D_\tau, \delta\lambda_\eta^{\mathrm{t}}, \delta\lambda_\eta^{\mathrm{c}}\right) \in \mathbb{R}^+ \times \mathbb{R}^+ \times \mathbb{R}^+ \times \mathbb{R}^+ \tag{41}$$

The first variation of action functional (**Eqn. (38)**) with respect to the six fundamental kinematic variables is defined via the following relation:

$$\begin{aligned}\delta\mathcal{E} = \mathcal{E}\big(&u_\eta + \delta u_\eta, u_{\tau_i} + \delta u_{\tau_i}, \lambda_\eta^{\mathrm{t}} + \delta\lambda_\eta^{\mathrm{t}}, \lambda_\eta^{\mathrm{c}} + \delta\lambda_\eta^{\mathrm{c}}, D_\eta \\ &+ \delta D_\eta, D_\tau + \delta D_\tau\big) - \mathcal{E}\left(u_\eta, u_{\tau_i}, \lambda_\eta^{\mathrm{t}}, \lambda_\eta^{\mathrm{c}}, D_\eta, D_\tau\right)\end{aligned} \tag{42}$$

The deformation process progresses depending on the increments in the kinematic quantities between two-time steps, i.e., t_i and t_{i-1}, which represent the current and previous times, respectively,

$$\begin{aligned}&\left(\Delta u_\eta, \Delta u_{\tau_i}, \Delta\lambda_\eta^{\mathrm{t}}, \Delta\lambda_\eta^{\mathrm{c}}, \Delta D_\eta, \Delta D_\tau\right)_{t_i} \\ &= \left(u_\eta, u_{\tau_i}, \lambda_\eta^{\mathrm{t}}, \lambda_\eta^{\mathrm{c}}, D_\eta, D_\tau\right)_{t_i} - \left(u_\eta, u_{\tau_i}, \lambda_\eta^{\mathrm{t}}, \lambda_\eta^{\mathrm{c}}, D_\eta, D_\tau\right)_{t_{i-1}}\end{aligned} \tag{43}$$

The increment energy is then expressed in the same manner:

$$\begin{aligned}\Delta\mathcal{E} = \mathcal{E}\big(&u_\eta + \Delta u_\eta, u_{\tau_i} + \Delta u_{\tau_i}, \lambda_\eta^{\mathrm{t}} + \Delta\lambda_\eta^{\mathrm{t}}, \lambda_\eta^{\mathrm{c}} + \Delta\lambda_\eta^{\mathrm{c}}, D_\eta \\ &+ \Delta D_\eta, D_\tau + \Delta D_\tau\big) - \mathcal{E}\left(u_\eta, u_{\tau_i}, \lambda_\eta^{\mathrm{t}}, \lambda_\eta^{\mathrm{c}}, D_\eta, D_\tau\right)\end{aligned} \tag{44}$$

The applicable hemi-variational principle (see Timofeev et al., 2021) where a detailed treatment is presented, is given as follows:

$$\begin{aligned}&\Delta\mathcal{E} \le \delta\mathcal{E} \quad \forall(\delta\mathbf{u}) \in AV_t, \\ &\left(\delta D_\eta, \delta D_\tau, \delta\lambda_\eta^{\mathrm{t}}, \delta\lambda_\eta^{\mathrm{c}}\right) \in \mathbb{R}^+ \times \mathbb{R}^+ \times \mathbb{R}^+ \times \mathbb{R}^+\end{aligned} \tag{45}$$

In light of the traditional variational approach, the governing equations, constitutive relations, and boundary conditions are presented in relation to the application of the hemi-variational approach as follows:

$$\operatorname{div}(\mathbb{S}) + \mathbf{b}^{\mathrm{ext}} = 0 \quad \forall \mathbf{X} \in \mathcal{B}, \tag{46}$$

$$\mathbb{S} = \mathbb{C}\boldsymbol{G} + \mathbb{L}\boldsymbol{G}^2 + \mathbb{N}\boldsymbol{G}^3 + \mathbb{P} \quad \forall \mathbf{X} \in \mathcal{B}, \tag{47}$$

$$\mathbb{S}\mathbf{n} = \mathbf{t}^{\mathrm{ext}} \quad \forall \mathbf{X} \in \partial_{\mathbf{t}}\mathcal{B} \tag{48}$$

here, while $\mathbb{S}$ presents the stress tensor, $\mathbf{n}$ denotes the outward unit normal vector to the domain boundary. In this paper, only homogeneous deformations are examined, i.e., the strain gradient terms are not included, $\boldsymbol{G}$ is a constant strain with respect to $\mathbf{X} \in \mathcal{B}$, and the external body force $\mathbf{b}^{\mathrm{ext}}$ is null. This implies that the divergence of $\mathbb{S}$ in **Eqn. (46)** is directly satisfied for $\mathbf{X} \in \mathcal{B}$, due to both the null external body force and the elastic stiffnesses in **Eqns. (27)–(30)** are independent of the configuration.

Further, the following Karush-Kuhn-Tucker (KKT)-type conditions are derived as follows:

$$\begin{aligned}\Big\{&-\frac{1}{2}k_\eta\left(u_\eta - \lambda_\eta^{\mathrm{t}} + \lambda_\eta^{\mathrm{c}}\right)^2 - \frac{1}{4}k_{\eta\eta}\left(u_\eta - \lambda_\eta^{\mathrm{t}} + \lambda_\eta^{\mathrm{c}}\right)^4 \\ &+ \frac{1}{2}k_\eta\left(B_\eta\right)^2\left[\tan\left(\frac{\pi}{2}\tilde{D}_\eta\right)\right]^2 - 2\left(1-\tilde{D}_\eta\right)\left(\sigma_\eta^{\mathrm{t}}\lambda_\eta^{\mathrm{t}} + \sigma_\eta^{\mathrm{c}}\lambda_\eta^{\mathrm{c}}\right. \\ &\left.+ \sigma_{\eta\eta}^{\mathrm{t}}(\lambda_\eta^{\mathrm{t}})^2 + \sigma_{\eta\eta}^{\mathrm{c}}(\lambda_\eta^{\mathrm{c}})^2 + \sigma_{\eta\eta}^{\mathrm{tc}}\lambda_\eta^{\mathrm{t}}\lambda_\eta^{\mathrm{c}}\right)\Big\}\Delta D_\eta = 0\end{aligned} \tag{49}$$

$$\left\{-\frac{1}{2}k_\tau\left(u_\tau^2\right) + \frac{1}{2}k_\tau\left(B_\tau\right)^2\left(\log\left(1-\tilde{D}_\tau\right)\right)^2\right\}\Delta D_\tau = 0 \tag{50}$$

$$\begin{aligned}\Big\{&-k_\eta\left(u_\eta - \tilde{\lambda}_\eta^{\mathrm{t}} + \lambda_\eta^{\mathrm{c}}\right) - k_{\eta\eta}\left(u_\eta - \tilde{\lambda}_\eta^{\mathrm{t}} + \lambda_\eta^{\mathrm{c}}\right)^3 \\ &+ \left(1-D_\eta\right)\left(\sigma_\eta^{\mathrm{t}} + 2\sigma_{\eta\eta}^{\mathrm{t}}\tilde{\lambda}_\eta^{\mathrm{t}} + \sigma_{\eta\eta}^{\mathrm{tc}}\lambda_\eta^{\mathrm{c}}\right)\Big\}\Delta\lambda_\eta^{\mathrm{t}} = 0\end{aligned} \tag{51}$$

$$\begin{aligned}\Big\{&k_\eta\left(u_\eta - \lambda_\eta^{\mathrm{t}} + \tilde{\lambda}_\eta^{\mathrm{c}}\right) + k_{\eta\eta}\left(u_\eta - \lambda_\eta^{\mathrm{t}} + \tilde{\lambda}_\eta^{\mathrm{c}}\right)^3 \\ &+ \left(1-D_\eta\right)\left(\sigma_\eta^{\mathrm{c}} + 2\sigma_{\eta\eta}^{\mathrm{c}}\tilde{\lambda}_\eta^{\mathrm{c}} + \sigma_{\eta\eta}^{\mathrm{tc}}\lambda_\eta^{\mathrm{t}}\right)\Big\}\Delta\lambda_\eta^{\mathrm{c}} = 0\end{aligned} \tag{52}$$

The KKT-type conditions can be described concisely in relation to the four irreversible kinematic descriptors as follows:

$$\left\{D_\eta - \tilde{D}_\eta\left(u_\eta, \lambda_\eta^{\mathrm{t}}, \lambda_\eta^{\mathrm{c}}\right)\right\}\Delta D_\eta = 0 \tag{53}$$

$$\left\{D_\tau - \tilde{D}_\tau\left(u_\eta^{\mathrm{el}}, u_\tau\right)\right\}\Delta D_\tau = 0 \tag{54}$$

$$\left\{\lambda_\eta^{\mathrm{t}} - \tilde{\lambda}_\eta^{\mathrm{t}}\left(u_\eta, D_\eta, \lambda_\eta^{\mathrm{c}}\right)\right\}\Delta\lambda_\eta^{\mathrm{t}} = 0 \tag{55}$$

$$\left\{\lambda_\eta^{\mathrm{c}} - \tilde{\lambda}_\eta^{\mathrm{c}}\left(u_\eta, D_\eta, \lambda_\eta^{\mathrm{t}}\right)\right\}\Delta\lambda_\eta^{\mathrm{c}} = 0 \tag{56}$$

where $\tilde{D}_\tau$ is the threshold function expressed via

$$\tilde{D}_\tau\left(u_\eta^{\mathrm{el}}, u_\tau\right) = 1 - \exp\left(-\frac{u_\tau}{\tilde{B}_\tau\left(u_\eta^{\mathrm{el}}\right)}\right) = 1 - \exp\left(-\frac{u_\tau}{B_\tau}\right) \tag{57}$$

In **Eqns. (49)–(52)**, the threshold functions for the evolution of damage and plasticity variables are obtained by setting the equations in the curly braces to zero. Due to the quartic power of the elastic normal displacement $\boldsymbol{u}_{\boldsymbol{\eta}}^{\mathbf{el}}$, nonlinear equations arise from the first variation of the elastic energy equation (see **Eqn. (21)**) with respect to irreversible quantities. Therefore, a numerical effort is required and $\tilde{\boldsymbol{D}}_{\boldsymbol{\eta}}$, $\tilde{\boldsymbol{\lambda}}_{\boldsymbol{\eta}}^{\mathbf{t}}$, and $\tilde{\boldsymbol{\lambda}}_{\boldsymbol{\eta}}^{\mathbf{c}}$ are updated using the irreversible quantities from the previous time step as initial guesses in **Eqns. (49)**, **(51)**, and **(52)**, respectively. An iterative solution of the nonlinear equations, until a certain tolerance of $\mathbf{10^{-10}}$ is reached, provides the single root for each variable. Notably, the $\tilde{\boldsymbol{D}}_{\boldsymbol{\tau}}$ threshold function in **Eqn. (50)** is derived

analytically as given in **Eqn. (57)**. It is important to underline that the evolution of damage and plasticity depends on the distinction between the tension and compression conditions for normal stiffness in **Eqn. (21)** and characteristic damage displacements in **Eqns. (35)** and **(36)**. At the beginning of the deformation history, $\tilde{\boldsymbol{D}}_{\boldsymbol{\eta}}$, $\tilde{\boldsymbol{D}}_{\boldsymbol{\tau}}$, $\tilde{\boldsymbol{\lambda}}^{\mathbf{t}}_{\boldsymbol{\eta}}$, and $\tilde{\boldsymbol{\lambda}}^{\mathbf{c}}_{\boldsymbol{\eta}}$ are null and evolve. Most importantly, damage and plasticity (which are from a thermodynamic viewpoint entropic quantities) do not decrease over time; their evolution continues if and only if the threshold value of the current time step is higher than that of the previous time step. Otherwise, these variables remain constant and fixed at the previous time step. At the limits where the elastic normal displacement or normal displacement goes to infinity, normal and tangent damage increase asymptotically toward unity. However, having the damage variables reach a value of 1 is not desired because this nullifies the elastic stiffnesses, as clearly seen in **Eqns. (27)–(30)**. In **Eqns. (49)**, **(51)**, and **(52)**, the predicted behavior of these irreversible quantities under loading–unloading, including both $\boldsymbol{D}_{\boldsymbol{\eta}}$ and the coupling term $\boldsymbol{\sigma}^{\mathbf{tc}}_{\boldsymbol{\eta\eta}}$ between plasticity evolution, will be examined in the next section. Remarkably, the coupling term plays a crucial role with loading–unloading history under one-dimensional compression by activating the effects of plasticity evolution on each other when $\boldsymbol{\sigma}^{\mathbf{tc}}_{\boldsymbol{\eta\eta}} \neq 0$. Furthermore, the softening parameter $\boldsymbol{\sigma}^{\mathbf{t}}_{\boldsymbol{\eta\eta}}$ for tension and hardening parameter $\boldsymbol{\sigma}^{\mathbf{c}}_{\boldsymbol{\eta\eta}}$ for compression regularize the evolution of plastic deformation. Finally, note that the orientation-dependent evolution of the irreversible quantities is the same for all grains considered, regardless of which grain is selected within the material.

3. Results and discussion

3.1 One-dimensional compression loading conditions

As depicted in **Fig. 2(a)**, one-dimensional compression involves compressing granular material within a die (or oedometer) with a piston plunging in the axial direction. The material is completely confined within rigid boundaries on all other sides, including the lateral sides. The boundary conditions are schematically shown in **Fig. 2(b)**,

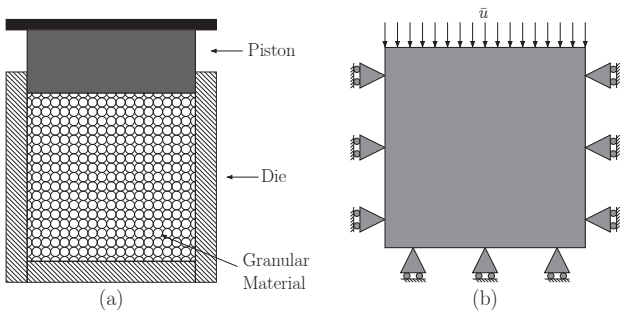

Fig. 2 **(a)** Schematic illustration of one-dimensional compression of granular materials. **(b)** Boundary conditions of one-dimensional compression.

in which the roller support is both in the 1-direction (2 side boundaries) and the bottom boundary of the specimen represents the rigid boundaries, while the axial compression is represented by displacement $\bar{u}$ in 2-direction (top boundary).

The numerical simulations were performed for a square specimen with an edge length of S by subjected to loading–unloading cycles. In the loading stage, the compressive displacement is first increased in the vertical direction to reach the maximum imposed displacement denoted by $\mathfrak{u}$. Subsequently, in the unloading process, we decrease the displacement, denoted by $u_2 = \mathfrak{u} - \bar{u}$ till the axial stress $\mathbb{S}_{22}$ reduces to zero. In this simulation, the lateral strain G_{11} and the shear strain G_{12} (or G_{21}) are zero, while the vertical strain $G_{22} = -G\,(G > 0)$ is calculated based on the displacement field according to **Eqn. (10)** as follows:

$$u_1 = 0, \quad u_2 = \frac{\bar{u}}{S}\mathrm{X}_2$$
$$\Rightarrow \mathbf{F} = \begin{pmatrix} 1 & 0 \\ 0 & 1+\dfrac{\bar{u}}{S} \end{pmatrix} \Rightarrow \boldsymbol{G} = \begin{pmatrix} 0 & 0 \\ 0 & \dfrac{1}{2}\left(\dfrac{\bar{u}}{S}\right)^2 + \dfrac{\bar{u}}{S} \end{pmatrix} \tag{58}$$

Based on the numerical solution of **Eqns. (49)**, **(51)**, and **(52)** and the analytical solution of **Eqn. (50)**, the evolution of damage and plasticity phenomena can be observed. Further, we calculate the elastic stiffness tensors, $\mathbb{C}_{ijab}$ (4^{th} - order), $\mathbb{L}_{ijabcd}$ (6^{th} - order), $\mathbb{N}_{ijabcdef}$ (8^{th} - order), and $\mathbb{P}_{ij}$ (2^{nd} - order), by utilizing **Eqns. (27)–(30)**. The vertical stress $\mathbb{S}_{22}$ and the lateral stress $\mathbb{S}_{11}$ are defined in **Eqn. (47)** based on the updated strain G_{22} by changing the compressive displacement $\bar{u}$ (see **Eqn. (58)**).

3.2 Dependence of parameters on initial density state and material type

The mechanical response under a uniaxial compression test was simulated for three granular material specimens derived from glass beads, Toyoura sand, and Masado sand, as described by Wu et al. (2016). Since a 2D theoretical formulation is utilized in this paper, an equivalence needs to be established with 3D axisymmetric experimental measurements, such that the stresses in 2D, which have a unit of measure of force per unit length, can be properly mapped to the experimental stress with a unit of measure of force per unit area. For this equivalence, we consider that the 2D model has a pseudo thickness, t, related to the cross-sectional area of typically cylindrical samples, such that the unit of measure remains consistent in the following manner:

$$\mathrm{t} = \sqrt{\pi r^2}, \quad \frac{\mathbb{S}_{22}}{\mathrm{t}} = \sigma_{22}\,(\mathrm{MPa}) \tag{59}$$

where r is the radius (typically 25.7 mm) of the specimen used in the experiments.

The model parameters can be determined by exploiting the relationship between the material elastic modulus and the void ratio e, as well as the identification of elastic modulus in terms of the microscale stiffness parameters given by Barchiesi et al. (2021). For the case of 2D granular system, the shear modulus is related to the microscale stiffness parameters as follows:

$$G_{2D} = \frac{L^2}{8}\left(k_\eta^c + 4k_\tau\right), \quad k_\tau = 0.1k_\eta^c \tag{60}$$

where the microscale tangential stiffness k_τ is assumed to be a fraction of the normal stiffness k_η^c, and L is the intergranular distance. Considering the experimental evidence and analyses presented by Chang et al. (1989), we assume that a simplified empirical relationship between the 2D shear modulus and the initial void ratio e can be expressed as follows:

$$G_{2D} = G_{emp} = \frac{A}{(e-0.2)^{1.8}} \tag{61}$$

where the void ratio, i.e., $e = V_V/V_S$, is determined as the ratio of the void volume V_V to the solid volume V_S, and A is the material-specific constant. As our reference material for parameter identification, we considered the experimental measurements of Toyoura sand presented by Wu et al. (2016). In these experiments, the initial void ratio of the specimen was close to 0.62 (which can also be considered as a mid-dense sand). It is reasonable to estimate that the shear modulus at the unloaded state or at the initial incipient loading is extremely low, as is easily observable from the initial part of stress–strain curves of granular materials under compression (see, for example, Figure 4 of Wu et al. (2016)). For our numerical calculations, we estimated an initial nominal shear modulus of 230 Pa such that the 2D shear modulus is $G_{2D} = 5.1 \times 10^3$ (J/m^2). For these experimental values of the initial void ratio and 2D shear modulus, the material-specific constant A is found to be 985 (J/m^2). Consequently, the normal stiffness k_η^c can be identified from **Eqn. (60)**.

For further discussion, the 2D shear modulus and normal compression stiffness for our reference Toyoura sand (mid-dense) specimen are symbolized with $\bar{G}_{2D}$ and $\bar{k}_\eta^c$, respectively, as given in **Table 1**. To define the material properties for the glass beads specimen (which behaved as a dense granular packing) and the Masado sand specimen (which behaved as a loose granular packing), the material stiffness parameter of the Toyoura sand specimen $\bar{k}_\eta^c$ were multiplied by 1.6 and 0.6, respectively. Given the initial 2D shear modulus, either the initial void ratio or the material-specific constant A for these specimens can be calculated using **Eqns. (60)** and **(61)**, respectively. It is noteworthy that the packing stiffness behavior is affected by both the particle stiffness and the initial void ratio (initial density states) in a similar manner (high particle stiffness or higher initial density typically yield stiffer packing behavior). In these cases, carefully controlled studies are needed to determine the relative influences of a myriad of characteristics of granular packing, including grain material types, grain surface characteristics, grain particle sizes, grain shapes, and packing density.

Further, we assign the compression characteristic damage displacement B_η^c using a trial-and-error approach through a fitting procedure. All other model parameters were assumed to be the same for all three specimens. **Table 1** gives the material-specific constant A, the shear modulus $\bar{G}_{2D}$, the stiffness $\bar{k}_\eta^c$, k_η^t, and k_τ, the characteristic damage displacements B_η^c, B_η^t, and $B_{\tau 0}$, the plasticity constitutive parameters σ_η^t, σ_η^c, $\sigma_{\eta\eta}^t$, $\sigma_{\eta\eta}^c$, and $\sigma_{\eta\eta}^{tc}$, the side length of a square specimen S, the average intergranular distance L, the regularization factors α and α_1, and the duffing stiffness coefficient k_{nn}.

In **Table 1**, we utilized non-dimensionalization to simplify the simulation system by reducing the number of independent parameters. Non-dimensionalization provides the way of material identification by rescaling the key characteristic parameters. This technique was utilized using the stiffness parameter k_η^c, the compression characteristic damage displacement B_η^c, and intergranular distance L in our numerical simulations, as depicted in **Table 1**.

3.3 One-dimensional compression: comparison with experimental results

To demonstrate the model's performance and its capability to replicate the macroscopic behavior in one-

Table 1 The simulation parameters for all specimens.

A (J/m^2)	$\bar{G}_{2D}$ (J/m^2) [see **Eqn. (60)**]	$\bar{k}_\eta^c$ (J/m^4)	k_η^t (J/m^4)	k_τ (J/m^4)	B_η^c (m)
985	5.1×10^3	2.93×10^8	$0.1\ k_\eta^c$	$0.1\ k_\eta^c$	$6.08\ L$
B_η^t (m)	$B_{\tau 0}$ (m)	σ_η^t (J/m^3)	σ_η^c (J/m^3)	$\sigma_{\eta\eta}^t$ (J/m^4)	$\sigma_{\eta\eta}^c$ (J/m^4)
$0.1\ B_\eta^c$	$0.1\ B_\eta^c$	0	$0.34\ k_\eta^c L$	$4.55\ k_\eta^c$	$227.27\ k_\eta^c$
$\sigma_{\eta\eta}^{tc}$ (J/m^4)	S (m)	L (m)	α (m)	α_1	k_{nn}
$-2.27\ k_\eta^c$	0.1	0.01	2.5×10^{-5}	10	5.0×10^4

dimensional compression of granular materials, a set of numerical simulations of the uniaxial test was performed for the three specimens discussed in the previous section. In **Fig. 3**, the model calculations and experimental results (from Figure 9 of Wu et al., 2016) were plotted for comparison. The experiments were performed in a cyclic manner to reach a maximum stress σ_{22} of 22.5 MPa with subsequent unloading to zero stress.

Fig. 3 illustrates that the glass beads specimen achieves the maximum stress at a lower strain and exhibits dense packing behavior. In contrast, the Masado sand specimen exhibits loose packing behavior, requiring a considerably higher strain to reach the same maximum stress level. The stiffening behavior observed in granular materials can be attributed to two primary mechanisms, one related to the stiffening of the grain-pair contact due to compression and the other related to the increased number of grain contacts due to the rearrangement process during the loading stage. At the beginning of the loading history (or at very low strain), the stiffening response rate is slow for all cases. For the glass beads specimen, significant stiffening is observed with maximum curvature at relatively low strain ($G = 0.02$–0.03) followed by a considerably steep slope of the stress–strain response at higher strains ($G > 0.05$). The steep stress–strain response indicates limited densification of glass bead packing, which is also attested by the relatively small change in the void ratio reported in the experimental data (see Figure 3 of Wu et al., 2016). Masado sand, which is considered a soft material, undergoes large deformation at the same stress level. Clearly, in this case, the rearrangement of particles accompanied by the collapse of granular structures as well as particle fragmentation plays an important role. In this case, two significant points must be considered. First, the large deformation of the specimen requires that finite deformation measures be used for describing the behavior as used in the current paper. Second, and importantly, this granular material experiences both considerable damage (defined as combined effects of grain-scale mechanisms, such as collapse/buckling of particle chains and loss of lateral support or confinement of grain neighborhoods) and plasticity (defined as the effective accumulation of plastic deformation resulting from grain breakage and grain-pair sliding and separation). It is interesting to observe that in this case, the stiffening effect is considerably gradual in comparison with the packing of both glass beads and Toyoura sand. The accumulation of damage, with likely loss of stiffness, and plasticity for the 3 specimens is visible from the unloading behavior. Clearly, for the case of the glass beads specimen, the proportion of dissipated energy is likely to be higher due to the plasticity mechanism than the loss of stiffness due to damage mechanism. In the case of the Toyoura and Masado sands, both mechanisms appear to contribute with plasticity being dominant. The close agreement between the model results and the experiments over the loading–unloading cycle is encouraging, given that only normal stiffness k_η^c was varied for the 3 specimens and all the other model parameters were adjusted according to the prescription in **Table 1**. The prediction, therefore, points to a nearly universal scaling with respect to the model parameters exhibited by granular materials of different types (or packing density).

Fig. 4 shows the void ratio e plotted against the logarithmically scaled vertical stress σ_{22} based upon model calculations and experimental observations (see Figure 3 of Wu et al., 2016). The model predictions provide an encouraging agreement with the experimental observations. It can be seen that the glass beads show the least change in the void ratio, whereas the Masado sand exhibits the largest change. A rapid decrease in the void ratio at high stress is typically indicative of grain crushing. This is particularly true for Masado sand, whose particle strength is known to be relatively low (Nakata et al., 2001) compared to glass beads and Toyoura sand. In **Fig. 5** we present the volumetric strain defined as $G_V = G_{11} + G_{22}$, and the vertical stress (based on Figure 4 of Wu et al., 2016) on a logarithmic scale for the three materials. Again, good agreement was achieved between the prediction and experimental observations of the volume compaction behavior of the three materials. It is worthwhile to reiterate that only one model

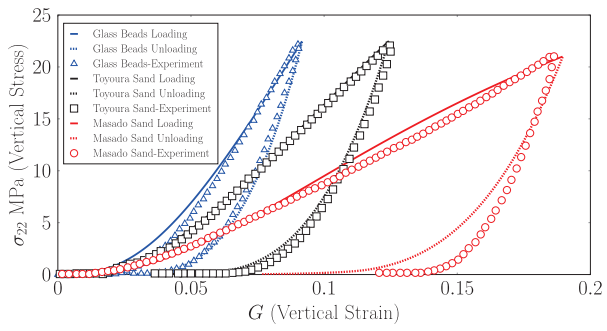

Fig. 3 Vertical stress σ_{22} versus vertical strain G for three different specimens by replicating the experimental observations based on the numerical simulations during the first loading–unloading cycle, reaching a maximum vertical stress of 22.5 MPa.

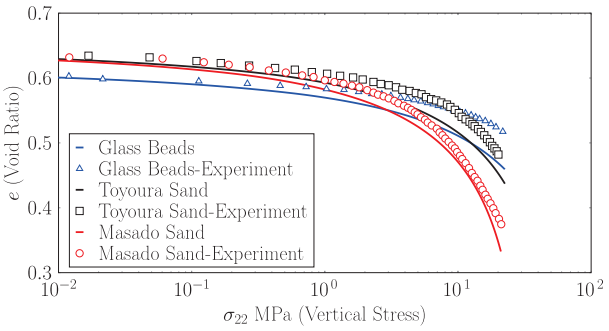

Fig. 4 Void ratio e versus vertical stress σ_{22} for the glass beads, Toyoura sand, and Masado sand specimens, based on numerical simulations during loading, reaching a maximum vertical stress of 22.5 MPa.

parameter was varied to obtain predictions for the three materials.

In Fig. 6, we investigate the relationship between the vertical and lateral stresses through the evolution of coefficient, $K_0 = \sigma_{11}/\sigma_{22}$, as the three materials undergo the loading–unloading cycle. During the loading phase, the lateral coefficient, which starts at around 0.15, under very low stress, exhibits a gradual but slight increase as the vertical stress rises. At the maximum stress, the coefficient

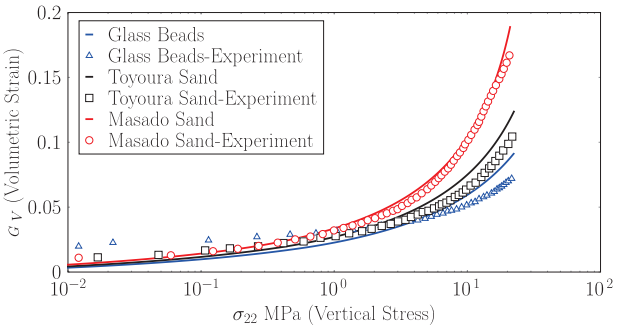

Fig. 5 Volumetric strain G_V versus vertical stress σ_{22} for glass beads, Toyoura sand, and Masado sand specimens, based on numerical simulations during loading, reaching a maximum vertical stress of 22.5 MPa.

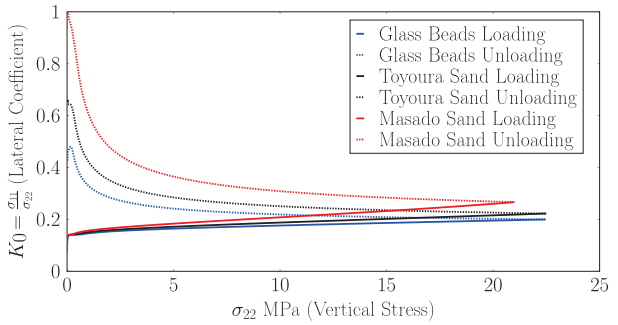

Fig. 6 Lateral coefficient K_0 versus vertical stress σ_{22} for glass beads, Toyoura sand, and Masado sand specimens, based on numerical simulations during the first loading–unloading cycle, reaching a maximum stress of 22.5 MPa.

K_0 for soft (loose) material is higher than that of the stiff (dense) material. In particular, the largest increase in K_0 value is observed for the Masado sand specimen. Under the boundary conditions shown in Fig. 2, an increase in the vertical stress inevitably causes an increase in the lateral stress for all specimens due to particle rearrangement and crushing and corresponds to the propensity to expand in the 1-direction. During the unloading stage, the lateral coefficient continues to increase gradually with unloading until the low-stress ranges where a rapid increase is predicted. The model predicted K_0 behavior follows the typical experimental observations for granular materials during both loading and unloading processes. We note, however, that the present model somewhat under predicts the rapid increase that is experimentally observed for the 3 materials (see Figure 15 of Wu et al., 2016). Such discrepancy can be remedied by further refinement of the grain-pair elastic energy functional to include a higher-order dependence on tangential displacement and the inclusion of plastic dissipation potential due to tangential displacement. It is also notable that the present energy-based approach is distinct from previous approaches that typically invoke macroscale phenomenological concepts, such as Mohr-Coulomb frictional models, with ad hoc modifications to explain such loading–unloading K_0 behavior. In this work, the predicted K_0 behavior emerges from microscale assumptions of elastic deformation energy and dissipation potential.

Figs. 7 and 8 further elaborate the predictive capacity of the present approach. Fig. 7 gives the axial loading–unloading behavior for the three granular materials with unloading performed at different loading levels. Fig. 8 gives the corresponding lateral stress versus axial stress behavior. Two observations are evident for all three materials. First, the materials stiffen as the loading level is raised; however, the stiffening rate is highest for glass beads, followed by Toyoura sand and then Masado sand. We also note that in Fig. 7c, at the large loading level, there is a tendency for stiffening to slow down, and likely

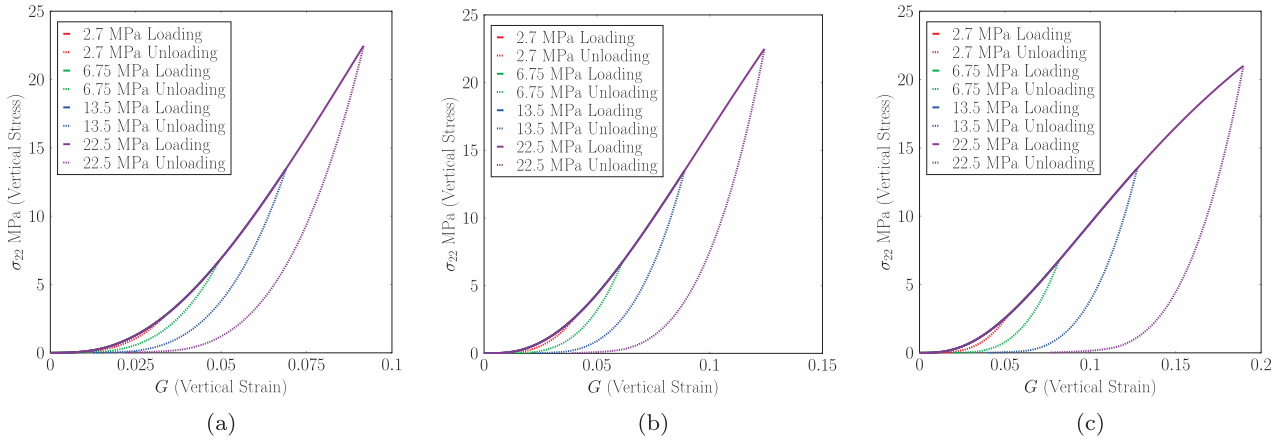

Fig. 7 Vertical stress σ_{22} versus vertical strain G for glass beads **(a)**, Toyoura sand **(b)**, and Masado sand **(c)** specimens based on numerical simulations during the first loading–unloading cycle, each reaching different maximum stresses.

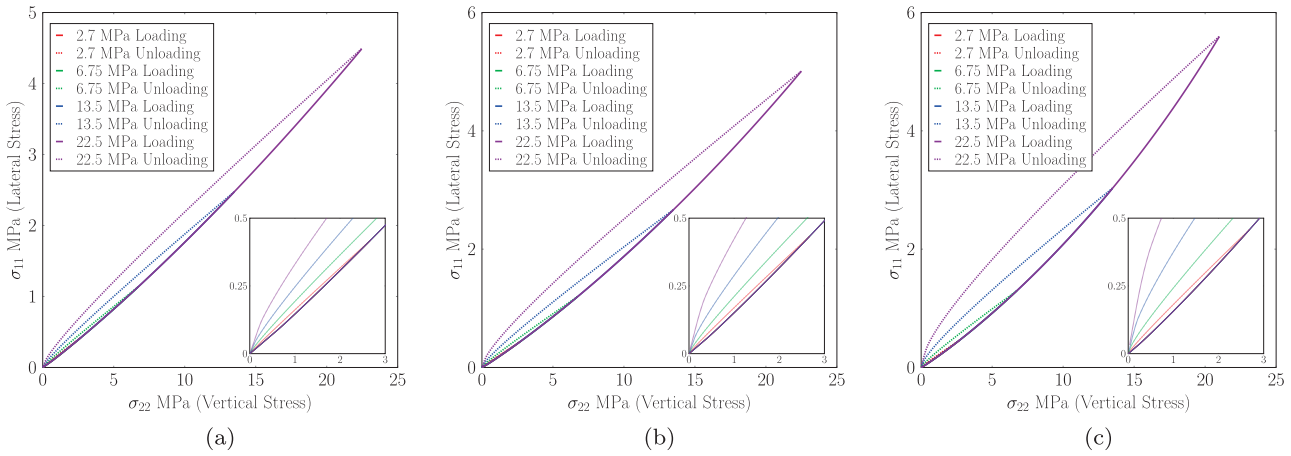

Fig. 8 Lateral stress σ_{11} versus vertical stress σ_{22} for glass beads **(a)**, Toyoura sand **(b)**, and Masado sand **(c)** specimens based on numerical simulations during the first loading–unloading, each reaching different maximum stresses.

transitioning to softening. Such a transition to softening has been observed at large loading levels in classical experiments (Hendron, 1963). Second, the dissipated energy, as indicated by the area of the loading–unloading loop, increases with loading level, however, the dissipation is the highest for Masado sand, followed by Toyoura sand and glass bead. It is clear that not only glass bead particles have higher stiffness and failure strength than the two sands, but also that the packing density of almost monodispersed glass beads is high. In contrast, it is likely that the particle stiffness/strength as well as the packing density of the more polydispersed sands exhibit lower. The model parameters used in the prediction reflect the particle and packing characteristics. The consequence of these characteristics is the different stiffening behavior and energy dissipation predicted for the three granular materials. It is remarkable that the predicted results are confirmed by the experimental observations, both for the vertical stress–strain response shown in **Fig. 7** and lateral stress versus vertical stress responses in **Fig. 8** (see also Figures 6–8 of Wu et al., 2016).

3.4 One-dimensional compression: parametric study

The nearly universal scaling observed in comparison with the model predictions in experiments was exploited to perform a suite of parametric study under one loading–unloading cycle as well as under repeated loading–unloading cycles. In these parametric studies, we also examined the behavior of lateral stress during 1D compression as well as microscale quantities including the directional evolution of grain-pair elastic energy and the grain-pair dissipation parameters of damage and plasticity. These parametric studies are interpreted as those for specimens with three different density states following from the discussion in the previous section related to the experimental behavior.

3.4.1 Scaling in loading–unloading cycle for one-dimensional compression

Fig. 9a plots the vertical stress $\mathbb{S}_{22}$ against the vertical strain G responses for three specimens (denoted as dense, mid-dense and loose) under loading–unloading cycles. During the simulations, a maximum displacement of $\bar{u} \simeq 0.01$ m is applied along the vertical direction, until a strain $G = 0.1$ was achieved. As expected, the loose specimen exhibits the lowest resistance at the same compaction compared with the dense specimen. As noted above, the compaction behavior can be scaled by considering either the particle stiffness or the initial void ratio (initial density states). In this study, the three density states were achieved by simply varying the particle stiffness k_η^c. In **Fig. 9b**, we present the normalized vertical stress $\tilde{\mathbb{S}}_{22}$ $(= \mathbb{S}_{22} / k_\eta^c L^2)$ versus the vertical strain G behavior where the vertical stress normalization is obtained by dividing the stress values by the product of material stiffness (k_η^c) and squared intergranular distance (L), i.e., $k_\eta^c L^2$, resulting in a non-dimensional quantity in terms of the unit of measure. We can observe that all curves merge into one, suggesting that universal scaling for 1D compression is possible. It is particularly noteworthy that the model parameters can be categorized into the equivalence class based on the stiffness k_η^c and intergranular distance to explain the scaling. Further, it is notable that the stiffness k_η^c represents not only the stiffness of a grain pair isolated from the assembly, but also the effect of the neighboring grain packing (see also the discussion in Misra and Poorsolhjouy (2017)). In this sense, the model parameters in our presented approach represent the effect of the neighboring grain packing on the grain-pair behavior. Therefore, such an effective grain-pair representation is different from that used in discrete models of granular materials.

Fig. 10 presents the corresponding lateral stress $\mathbb{S}_{11}$ versus the vertical stress $\mathbb{S}_{22}$ for the three cases. The lateral stress results from the tendency of specimens to dilate

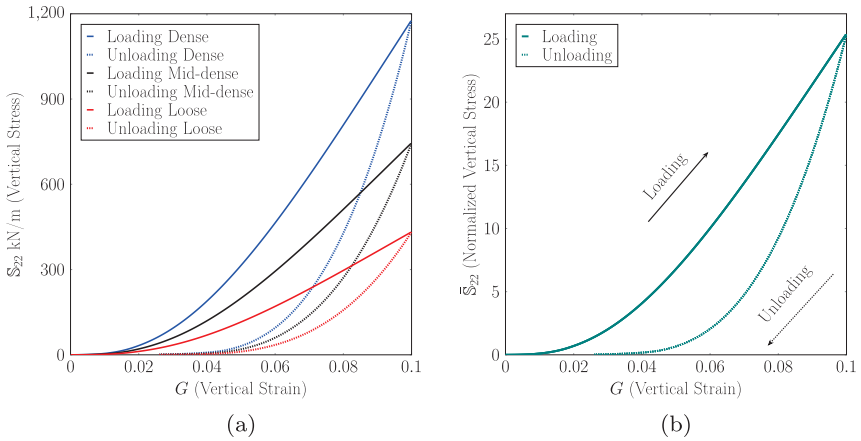

Fig. 9 **(a)** Vertical stress $\mathbb{S}_{22}$ versus vertical strain G obtained from numerical simulations for dense, mid-dense, and loose specimens during the first loading–unloading cycle, reaching a maximum strain of G=0.1. **(b)** Normalized vertical stress $\bar{\mathbb{S}}_{22}$ versus vertical strain G obtained from numerical simulations for dense, mid-dense, and loose specimens during the first loading–unloading cycle, reaching a maximum strain of G=0.1. The stress normalization is performed by dividing the vertical stress $k_\eta^c L^2$.

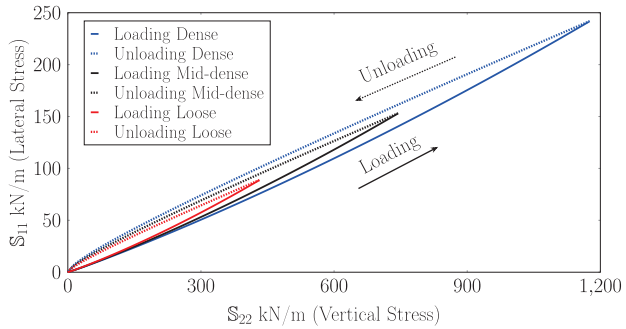

Fig. 10 Lateral stress $\mathbb{S}_{11}$ versus vertical stress $\mathbb{S}_{22}$ obtained from numerical simulations for dense, mid-dense, and loose specimens during the first loading–unloading until reaching a maximum strain (G = 0.1).

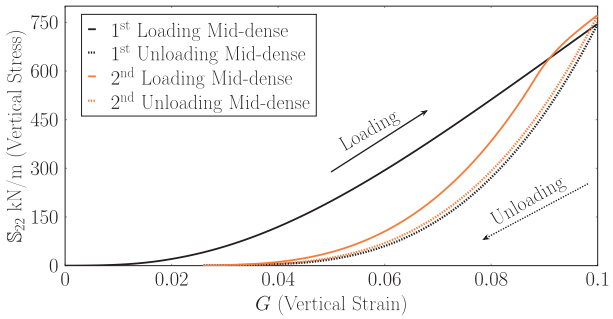

Fig. 11 Vertical stress $\mathbb{S}_{22}$ versus vertical strain G obtained from numerical simulations for a mid-dense specimen at maximum strain (G = 0.1) during two cyclic loading–unloading.

laterally due to positive Poisson's effect and the confining lateral boundary conditions as the vertical stress increases. It is notable that the vertical stress, typically, increases at a faster rate than the lateral stress, although with a minor slowdown. Upon unloading, the rate at which the vertical stress decreases is typically faster, such that the lateral stress near complete unloading is higher than the vertical stress, which also agrees with classical experimental observations (Hendron, 1963). The resulting lateral-to-vertical stress ratio (also known as coefficient of later pressure $K_0 = \sigma_{11}/\sigma_{22}$) can become greater than 1 during unloading. It is notable that the rate of change of the vertical and lateral stress is determined by the directional evolution of damage and plasticity, which will be examined in detail in a later section.

3.4.2 Repeated loading–unloading under one-dimensional compression

Fig. 11 shows the stress–strain response for a mid-dense specimen under one-dimensional compression for repeated loading–unloading over 2-cycles: 1st Loading, 1st Unloading, 2nd Loading, and 2nd Unloading. Under 1D compression, the material experiences most damage and plasticity during the 1st load–unload cycle. During the 2nd loading, the initial response is noticeably softer compared to the 1st loading. However, the stiffening proceeds rapidly until the original stress–strain curve is intercepted, beyond which the response follows the virgin or 1st loading curve, as widely observed in experimental studies of granular geomaterials (see, for example, Lambe and Whitman, 1991). It is encouraging to observe that the 2nd unload curve follows the 1st unload curve as is typically observed. Finally, as expected, we observe that the energy dissipation in the 2nd loading–unloading cycle, reckoned as the area of the load–unload loop, is considerably smaller than the 1st cycle or virgin loading as the material undergoes less damage/plastic evolution.

3.4.3 Directional evolution of elastic energy, damage, and plasticity

A key aspect of the proposed model based on granular micromechanics is that the discrete nature of granular materials is accounted for by the effective behavior of the grain pair. Thus, the evolution of elastic energy, damage,

and plasticity of grain pairs oriented in various spatial directions can reveal important insights into the emerging macroscale response of granular materials. Fig. 12 shows the polar plots of the elastic energy evolution of effective grain pairs oriented in different directions for the simulations described in the previous section. The loading–unloading–reloading stages were divided into four different vertical strain intervals in columns (i), (ii), (iii), and (iv). Further, for each polar plot, 10 equal steps within the vertical strain range were considered. We observed that the elastic energy exhibits a gradual increase in all directions during 1st loading with a larger increase, as expected, in grain pairs oriented closer to the direction of loading (vertical or 2-direction). Since the grain-pair elastic energy includes a quartic dependency upon the grain-pair normal displacement, an anisotropic stiffening in the loading direction evolves, which is reflected in the directional distribution of the elastic energy. Clearly, the direction of the larger grain-pair energy results reflects a higher elastic stiffness in that direction. In this sense, GMA provides the advantage of directly connecting the microscale stiffening to the emergent macroscale stiffening of the granular material.

During unloading, a part of the stored elastic energy is recovered, as seen by the reduction of elastic energy in the vertical direction (neighboring orientation of 90°) as seen in row 2 of Fig. 12, in which the unloading proceeds from right to left. It is interesting to note that the vertical directions unload faster, in contrast to almost uniform rate of increase in all directions during loading. This phenomenon is particularly visible during unloading at strains below 0.05. Such elastic energy evolution for the effective grain pairs is influenced by the assumed dissipation behavior in the tangential direction, which is only due to damage. In particular, for grain-pair orientations inclined with respect to the principal loading direction (vicinity of 45°, 135°, 225°, and 315°, respectively), the elastic displacement, especially in the tangential direction, decreases at a slower rate. Consequently, the elastic energy reduction in these inclined directions is more gradual than in the vertical direction. In the subsequent load–unload cycle, a similar phenomenon is observed, but with nuanced variation influenced by both the directional evolution of damage and plastic displacements, as depicted in Figs. 13–16. During loading, the normal damage (Fig. 13) and plastic multiplier (Fig. 15) evolve faster in the direction of principal loading (neighboring orientation of 90°). The result is that the normal stiffness in these directions is reduced. In addition, the elastic displacement in these directions decreases at a faster rate during unloading and grows at a slower rate during the 2nd loading. As a consequence, the evolution of elastic energy takes a flat 8 shape, as shown in the 3rd row of Fig. 12.

It is further notable that the directional evolution of damage and plasticity leads to the induction of anisotropy as the loading progresses. The anisotropy development is also influenced by the quartic dependence of the effective grain-pair elastic energy on the elastic normal displacement u_η^{el} with the duffing stiffness $k_{\eta\eta}$ in Eqn. (25). Undoubtedly, the directional evolution of microscale elastic energy,

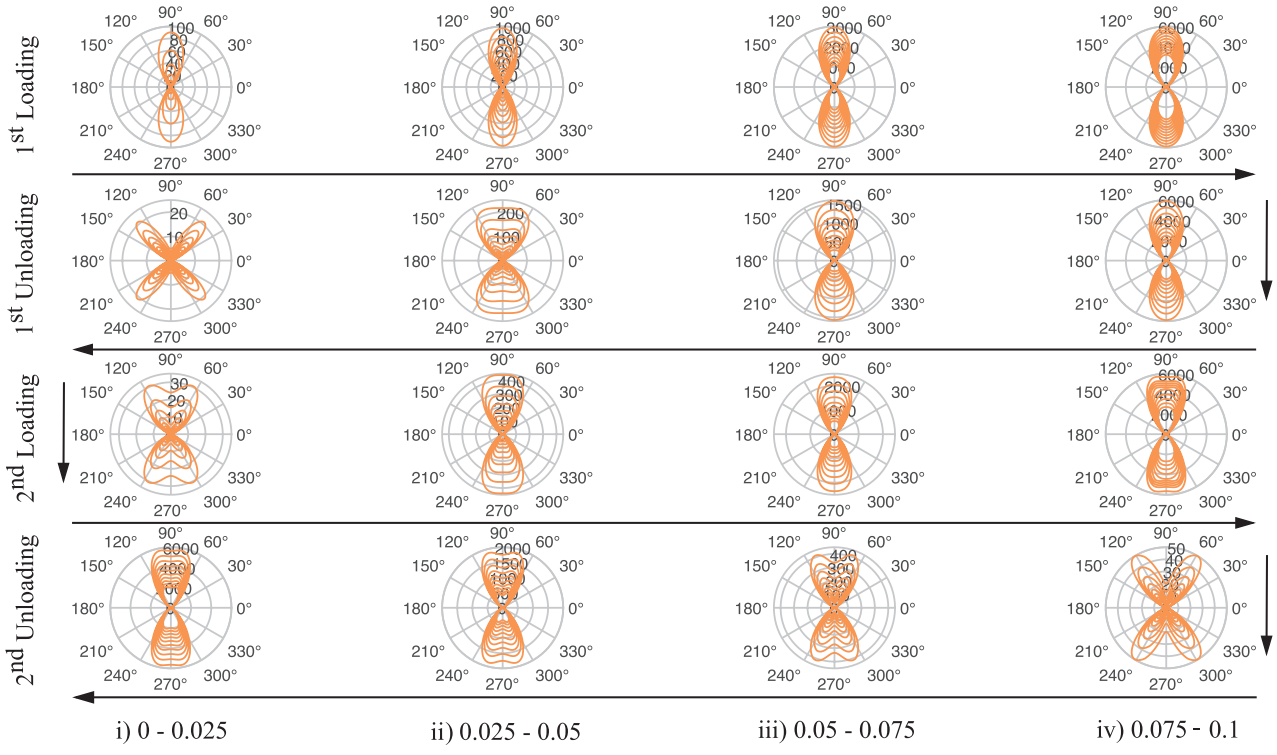

Fig. 12 Polar plots of elastic energy U for a mid-dense specimen during cyclic loading–unloading under one-dimensional compression at different strain intervals.

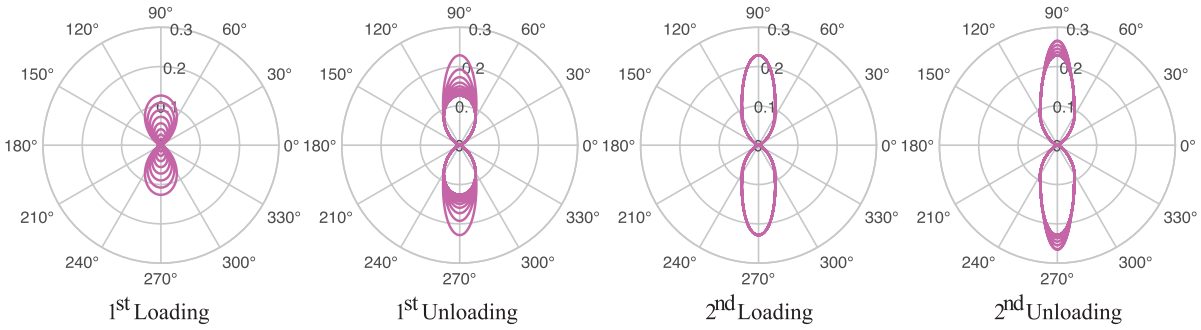

Fig. 13 Polar plots of normal damage D_η for a mid-dense specimen during cyclic loading–unloading under one-dimensional compression.

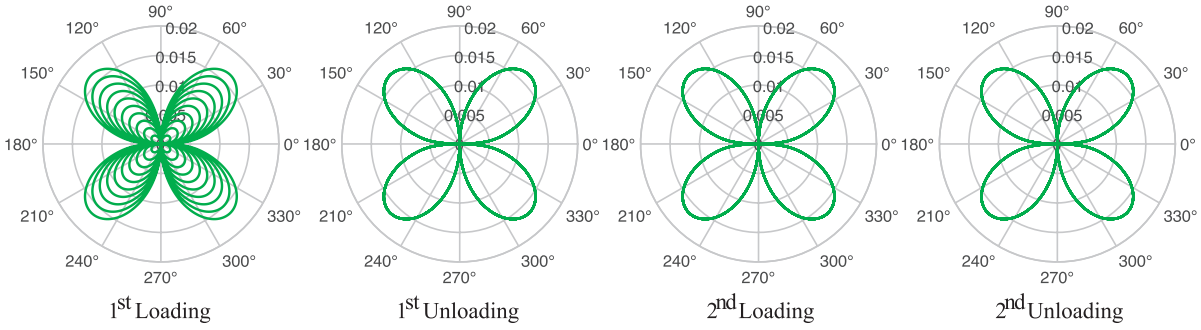

Fig. 14 Polar plots of tangential damage D_τ for a mid-dense specimen during cyclic loading–unloading under one-dimensional compression.

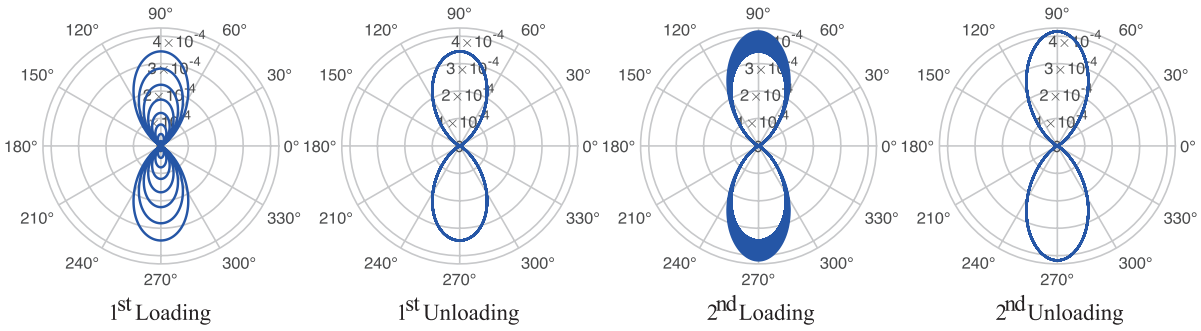

Fig. 15 Polar plots of the compression plastic multiplier λ_η^c for a mid-dense specimen during cyclic loading–unloading under one-dimensional compression.

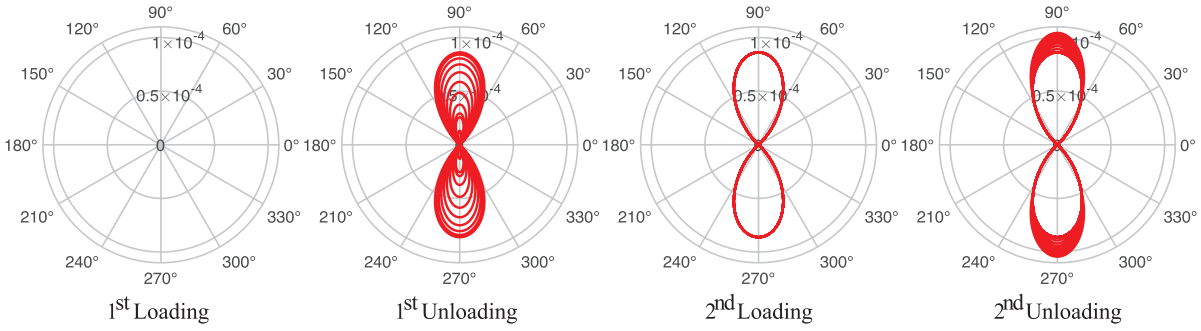

Fig. 16 Polar plots of the tension plastic multiplier λ_η^t for a mid-dense specimen during cyclic loading–unloading under one-dimensional compression.

damage, and plasticity, as illustrated by the polar plots, play an important role in understanding the hardening/softening behavior, loading–unloading path dependency, and deformation mechanisms.

4. Conclusion

The novel contribution of this study is to apply the granular micromechanics approach (GMA) for developing a continuum model that replicates the experimental

observations in one-dimensional compression according to constituent grain stiffness or different initial density states. We have shown that the emergent macroscale behavior can be explored by utilizing properly conceived damage-elasto-plastic spring elements in the normal and tangential directions, which represent the effective behavior of grain pairs in a granular material. In the presented approach, damage is defined as the loss of stiffness, structural integrity, and lateral support due to the interplay of microstructural mechanisms such as rotation/sliding of particles and compaction, while plasticity is defined as the cumulative irreversible displacements due to grain rearrangement, grain fracture and crushing, and buckling/collapse of particle chains. The elastic energy functionals and the dissipation potential of the grain-pair damage-elasto-plastic spring elements have been modified from the previous works (Placidi et al., 2021, 2024; Yilmaz et al., 2024, 2025) by implementing a quartic dependence on the elastic normal displacement into the elastic energy and a coupling term into plastic dissipation potential.

The model was applied to simulate the one-dimensional compression response. The results were obtained not only as the stress–strain responses but also as polar plots of the effective grain-pair elastic energy and coupled damage and plasticity when subjected to uniaxial compressive displacement. The stiff and soft specimens were proportionally determined according to the material stiffness of the mid-dense specimen and their stress–strain responses varied at the same rate. Typical experimental test data and predicted results were compared for validating the model. The model results were in conformity with the initial linear behavior, evident curvature, secondary linear increase, and peak stress. The model was able to correctly predict the observed variation of void ratio and volume strain during loading. In addition, the model was able to replicate the lateral-to-axial stress-ratio behavior under loading–unloading cycle and, more significantly, the growth of this ratio under unloading. A parametric study was conducted, which revealed that the one-dimensional compression behavior has universal scaling for different constituent grain types or packing density. The results of the parametric study were also used to investigate the directional evolution of elastic energy, damage and plasticity, during loading–unloading-reloading process.

In future work, path-dependent analysis can be simulated by implementing additional deformation mechanisms into the effective grain-pair elastic energy and dissipation potential. Additionally, the model can be refined by incorporating plasticity in the tangential direction and establishing coupling terms between normal and tangential irreversible quantities. The resultant GMA-based model can be applied to unravel the behavior under homogeneous deformations or under non-homogeneous conditions by implementation in finite element analysis. For instance, further advancements can be made in understanding the mechanical behavior of granular materials under various loading conditions by combining the findings of Placidi et al. (2021, 2024), Timofeev et al. (2021), and Yilmaz et al. (2024, 2025).

References

Abali B.E., Müller W.H., Eremeyev V.A., Strain gradient elasticity with geometric nonlinearities and its computational evaluation, Mechanics of Advanced Materials and Modern Processes, 1 (2015) 1–11. https://doi.org/10.1186/s40759-015-0004-3

Abali B.E., Müller W.H., dell'Isola F., Theory and computation of higher gradient elasticity theories based on action principles, Archive of Applied Mechanics, 87(9) (2017) 1495–1510. https://doi.org/10.1007/s00419-017-1266-5

Abali B.E., Yang H., Papadopoulos P., A computational approach for determination of parameters in generalized mechanics, in: Altenbach H., Müller W.H., Abali B.E. (Eds.), Higher Gradient Materials and Related Generalized Continua, Springer International Publishing, Cham, 2019, pp. 1–18, ISBN: 978-3030304065. https://doi.org/10.1007/978-3-030-30406-5_1

Aydin G., Sarar B.C., Yildizdag M.E., Abali B.E., Investigating infill density and pattern effects in additive manufacturing by characterizing metamaterials along the strain-gradient theory, Mathematics and Mechanics of Solids, 27(10) (2022) 2002–2016. https://doi.org/10.1177/10812865221100978

Bandara K., Ranjith P., Rathnaweera T., Wanniarachchi W., Yang S., Crushing and embedment of proppant packs under cyclic loading: an insight to enhanced unconventional oil/gas recovery, Geoscience Frontiers, 12(6) (2021) 100970. https://doi.org/10.1016/j.gsf.2020.02.017

Barchiesi E., Misra A., Placidi L., Turco E., Granular micromechanics-based identification of isotropic strain gradient parameters for elastic geometrically nonlinear deformations, Journal of Applied Mathematics and Mechanics, 101(11) (2021) e202100059. https://doi.org/10.1002/zamm.202100059

Bolton M., Nakata Y., Cheng Y., Micro- and macro-mechanical behaviour of DEM crushable materials, Géotechnique, 58(6) (2008) 471–480. https://doi.org/10.1680/geot.2008.58.6.471

Campbell C.S., Rapid granular flows, Annual Review of Fluid Mechanics, 22(1) (1990) 57–90. https://doi.org/10.1146/annurev.fl.22.010190.000421

Carrera A., Coop M., Lancellotta R., Influence of grading on the mechanical behaviour of Stava tailings, Géotechnique, 61(11) (2011) 935–946. https://doi.org/10.1680/geot.9.P.009

Chang C., Hicher P.Y., An elasto-plastic model for granular materials with microstructural consideration, International Journal of Solids and Structures, 42(14) (2005) 4258–4277. https://doi.org/10.1016/j.ijsolstr.2004.09.021

Chang C.S., Misra A., Theoretical and experimental study of regular packings of granules, Journal of Engineering Mechanics, 115(4) (1989) 704–720. https://doi.org/10.1061/(ASCE)0733-9399(1989)115:4(704)

Chang C.S., Sundaram S.S., Misra A., Initial moduli of particulated mass with frictional contacts, International Journal for Numerical and Analytical Methods in Geomechanics, 13(6) (1989) 629–644. https://doi.org/10.1002/nag.1610130605

Cheng Y., Nakata Y., Bolton M.D., Discrete element simulation of crushable soil, Geotechnique, 53(7) (2003) 633–641. https://doi.org/10.1680/geot.2003.53.7.633

Chong S.H., Santamarina J.C., Soil compressibility models for a wide stress range, Journal of Geotechnical and Geoenvironmental Engineering, 142(6) (2016) 06016003. https://doi.org/10.1061/(ASCE)GT.1943-5606.0001482

Chtourou H., Guillot M., Gakwaya A., Modeling of the metal powder compaction process using the cap model. Part I. Experimental material characterization and validation, International Journal of solids and Structures, 39(4) (2002a) 1059–1075.

https://doi.org/10.1016/S0020-7683(01)00255-4
Chtourou H., Gakwaya A., Guillot M., Modeling of the metal powder compaction process using the cap model. Part II: Numerical implementation and practical applications, International Journal of Solids and Structures, 39(4) (2002b) 1077–1096. https://doi.org/10.1016/S0020-7683(01)00256-6
Chung Y., Lin C., Chou P., Hsiau S., Mechanical behaviour of a granular solid and its contacting deformable structure under uni-axial compression–Part I: joint DEM–FEM modelling and experimental validation, Chemical Engineering Science, 144 (2016) 404–420. https://doi.org/10.1016/j.ces.2015.11.024
Cil M.B., Alshibli K.A., 3D assessment of fracture of sand particles using discrete element method, Géotechnique Letters, 2(3) (2012) 161–166. https://doi.org/10.1680/geolett.12.00024
Cil M.B., Alshibli K.A., 3D evolution of sand fracture under 1D compression, Géotechnique, 64(5) (2014) 351–364. https://doi.org/10.1680/geot.13.P.119
Cocks A., Sinka I., Constitutive modelling of powder compaction–I. Theoretical concepts, Mechanics of Materials, 39(4) (2007) 392–403. https://doi.org/10.1016/j.mechmat.2006.09.003
Cocks A.C., Constitutive modelling of powder compaction and sintering, Progress in Materials Science, 46(3–4) (2001) 201–229. https://doi.org/10.1016/S0079-6425(00)00017-7
Daouadji A., Hicher P.Y., Rahma A., An elastoplastic model for granular materials taking into account grain breakage, European Journal of Mechanics-A/Solids, 20(1) (2001) 113–137. https://doi.org/10.1016/S0997-7538(00)01130-X
de Bono J.P., McDowell G.R., Discrete element modelling of one-dimensional compression of cemented sand, Granular Matter, 16 (2014) 79–90. https://doi.org/10.1007/s10035-013-0466-0
dell'Isola F., Andreaus U., Placidi L., At the origins and in the vanguard of peridynamics, non-local and higher-gradient continuum mechanics: an underestimated and still topical contribution of Gabrio Piola, Mathematics and Mechanics of Solids, 20(8) (2015) 887–928. https://doi.org/10.1177/1081286513509811
dell'Isola F., Eugster S.R., Fedele R., Seppecher P., Second-gradient continua: from Lagrangian to Eulerian and back, Mathematics and Mechanics of Solids, 27(12) (2022) 2715–2750. https://doi.org/10.1177/10812865221078822
dell'Isola F., Misra A., Principle of virtual work as foundational framework for metamaterial discovery and rational design, Comptes Rendus Mécanique, 351(S3) (2023) 65–89. https://doi.org/10.5802/crmeca.151
dell'Isola F., Seppecher P., Placidi L., Barchiesi E., Misra A., Least action and virtual work principles for the formulation of generalized continuum models, in: dell'Isola F., Steigmann D.J. (Eds.), Discrete and Continuum Models for Complex Metamaterials, Cambridge University Press, Cambridge, 2020, pp. 327–394, ISBN: 978-1107087736. https://doi.org/10.1017/9781316104262.010
Einav I., Breakage mechanics—Part I: theory, Journal of the Mechanics and Physics of Solids, 55(6) (2007a)1274–1297. https://doi.org/10.1016/j.jmps.2006.11.003
Einav I., Breakage mechanics—Part II: modelling granular materials, Journal of the Mechanics and Physics of Solids, 55(6) (2007b) 1298–1320. https://doi.org/10.1016/j.jmps.2006.11.004
Eremeyev V.A., Cazzani A., dell'Isola F., On nonlinear dilatational strain gradient elasticity, Continuum Mechanics and Thermodynamics, 33 (2021) 1429–1463. https://doi.org/10.1007/s00161-021-00993-6
Eremeyev V.A., dell'Isola F., Boutin C., Steigmann D., Linear pantographic sheets: existence and uniqueness of weak solutions, Journal of Elasticity, 132 (2018) 175–196. https://doi.org/10.1007/s10659-017-9660-3
Fabbrocino F., Carpentieri G., Three-dimensional modeling of the wave dynamics of tensegrity lattices, Composite Structures, 173 (2017) 9–16. https://doi.org/10.1016/j.compstruct.2017.03.102
Fedele R., Piola's approach to the equilibrium problem for bodies with second gradient energies. Part I: first gradient theory and differential geometry, Continuum Mechanics and Thermodynamics, 34(2) (2022a) 445–474. https://doi.org/10.1007/s00161-021-01064-6
Fedele R., Approach à la Piola for the equilibrium problem of bodies with second gradient energies. Part II: variational derivation of second gradient equations and their transport, Continuum Mechanics and Thermodynamics, 34(5) (2022b) 1087–1111. https://doi.org/10.1007/s00161-022-01100-z
Fedele R., Placidi L., Fabbrocino F., A review of inverse problems for generalized elastic media: formulations, experiments, synthesis, Continuum Mechanics and Thermodynamics, 36 (2024) 1413–1453. https://doi.org/10.1007/s00161-024-01314-3
García X., Medina E.A., Hysteresis effects studied by numerical simulations: cyclic loading–unloading of a realistic sand model, Geophysics, 71(2) (2006) F13–F20. https://doi.org/10.1190/1.2181309
Giorgio I., dell'Isola F., Andreaus U., Misra A., An orthotropic continuum model with substructure evolution for describing bone remodeling: an interpretation of the primary mechanism behind Wolff's law, Biomechanics and Modeling in Mechanobiology, 22(6) (2023) 2135–2152. https://doi.org/10.1007/s10237-023-01755-w
Giorgio I., Hild F., Gerami E., dell'Isola F., Misra A., Experimental verification of 2D Cosserat chirality with stretch-micro-rotation coupling in orthotropic metamaterials with granular motif, Mechanics Research Communications, 126 (2022) 104020. https://doi.org/10.1016/j.mechrescom.2022.104020
Goldhirsch I., Rapid granular flows, Annual Review of Fluid Mechanics, 35(1) (2003) 267–293. https://doi.org/10.1146/annurev.fluid.35.101101.161114
Grande E., Milani G., Formisano A., Ghiassi B., Fabbrocino F., Bond behaviour of FRP strengthening applied on curved masonry substrates: numerical study, International Journal of Masonry Research and Innovation, 5(3) (2020) 303–320. https://doi.org/10.1504/IJMRI.2020.107980
Grindrod P.M., Heap M.J., Fortes A.D., Meredith P.G., Wood I.G., Trippetta F., Sammonds P.R., Experimental investigation of the mechanical properties of synthetic magnesium sulfate hydrates: Implications for the strength of hydrated deposits on Mars, Journal of Geophysical Research: Planets, 115(E6) (2010). https://doi.org/10.1029/2009JE003552
Güner F., Cora Ö.N., Sofuoğlu H., Numerical modeling of cold powder compaction using multi particle and continuum media approaches, Powder Technology, 271 (2015) 238–247. https://doi.org/10.1016/j.powtec.2014.11.008
Hanley K.J., O'Sullivan C., Huang X., Particle-scale mechanics of sand crushing in compression and shearing using DEM, Soils and Foundations, 55(5) (2015) 1100–1112. https://doi.org/10.1016/j.sandf.2015.09.011
Harireche O., McDowell G., Discrete element modelling of cyclic loading of crushable aggreates, Granular Matter, 5 (2003) 147–151. https://doi.org/10.1007/s10035-003-0143-9
Hendron Jr A.J., The Behavior of Sand in One-Dimensional Compression, University of Illinois at Urbana-Champaign, 1963. <https://apps.dtic.mil/sti/citations/AD0424192> accessed Oct 21 2025.
Jagota A., Dawson P., Jenkins J., An anisotropic continuum model for the sintering and compaction of powder packings, Mechanics of Materials, 7(3) (1988) 255–269. https://doi.org/10.1016/0167-6636(88)90024-5
Jiang M., Li T., Hu H., Thornton C., DEM analyses of one-dimensional compression and collapse behaviour of unsaturated structural loess, Computers and Geotechnics, 60 (2014) 47–60. https://doi.org/10.1016/j.compgeo.2014.04.002
Lambe T.W., Whitman R.V., Soil Mechanics, John Wiley & Sons, 1991, ISBN: 978-0471511922.
Leuenberger H., Rohera B.D., Fundamentals of powder compression. I. The compactibility and compressibility of pharmaceutical powders, Pharmaceutical Research, 3 (1986) 12–22. https://doi.org/10.1023/A:1016364613722
Mancusi G., Fabbrocino F., Feo L., Fraternali F., Size effect and dynamic properties of 2D lattice materials, Composites Part B: Engineering, 112 (2017) 235–242. https://doi.org/10.1016/j.compositesb.2016.12.026
McDowell G.R., de Bono J.P., On the micro mechanics of one-dimensional normal compression, Géotechnique, 63(11) (2013) 895–908. https://doi.org/10.1680/geot.12.P.041

Michrafy A., Ringenbacher D., Tchoreloff P., Modelling the compaction behaviour of powders: application to pharmaceutical powders, Powder Technology, 127(3) (2002) 257–266. https://doi.org/10.1016/S0032-5910(02)00119-5

Minh N., Cheng Y., A DEM investigation of the effect of particle-size distribution on one-dimensional compression, Géotechnique, 63(1) (2013) 44–53. https://doi.org/10.1680/geot.10.P.058

Misra A., Huang S., Micromechanical stress–displacement model for rough interfaces: effect of asperity contact orientation on closure and shear behavior, International Journal of Solids and Structures, 49(1) (2012) 111–120. https://doi.org/10.1016/j.ijsolstr.2011.09.013

Misra A., Marangos O., Rock-joint micromechanics: relationship of roughness to closure and wave propagation, International Journal of Geomechanics, 11(6) (2011) 431–439. https://doi.org/10.1061/(ASCE)GM.1943-5622.0000021

Misra A., Placidi L., dell'Isola F., Barchiesi E., Identification of a geometrically nonlinear micromorphic continuum via granular micromechanics, Zeitschrift für angewandte Mathematik und Physik, 72 (2021) 157. https://doi.org/10.1007/s00033-021-01587-7

Misra A., Poorsolhjouy P., Elastic behavior of 2D grain packing modeled as micromorphic media based on granular micromechanics, Journal of Engineering Mechanics, 143(1) (2017) C4016005. https://doi.org/10.1061/(ASCE)EM.1943-7889.0001060

Misra A., Yang Y., Micromechanical model for cohesive materials based upon pseudo-granular structure, International Journal of Solids and Structures, 47(21) (2010) 2970–2981. https://doi.org/10.1016/j.ijsolstr.2010.07.002

Mohan S., Compression physics of pharmaceutical powders: a review, International Journal of Pharmaceutical Sciences and Research, 3(06) (2012) 1580–1592. https://doi.org/10.13040/IJPSR.0975-8232.3(6).1580-92

Monkul M.M., Ozden G., Compressional behavior of clayey sand and transition fines content, Engineering Geology, 89(3–4) (2007) 195–205. https://doi.org/10.1016/j.enggeo.2006.10.001

Nakata Y., Kato Y., Hyodo M., Hyde A.F., Murata H., One-dimensional compression behaviour of uniformly graded sand related to single particle crushing strength, Soils and Foundations, 41(2) (2001) 39–51. https://doi.org/10.3208/sandf.41.2_39

Niesz D.E., A review of ceramic powder compaction, KONA Powder and Particle Journal, 14 (1996) 44–51. https://doi.org/10.14356/kona.1996009

Onate E., Rojek J., Combination of discrete element and finite element methods for dynamic analysis of geomechanics problems, Computer Methods in Applied Mechanics and Engineering, 193(27–29) (2004) 3087–3128. https://doi.org/10.1016/j.cma.2003.12.056

Park S.J., Han H.N., Oh K.H., Lee D.N., Model for compaction of metal powders, International Journal of Mechanical Sciences, 41(2) (1999) 121–141. https://doi.org/10.1016/S0020-7403(98)00022-8

Pastor M., Zienkiewicz O., Chan A., Generalized plasticity and the modelling of soil behaviour, International Journal for Numerical and Analytical Methods in Geomechanics, 14(3) (1990) 151–190. https://doi.org/10.1002/nag.1610140302

Placidi L., A variational approach for a nonlinear one-dimensional damage-elasto-plastic second-gradient continuum model, Continuum Mechanics and Thermodynamics, 28 (2016) 119–137. https://doi.org/10.1007/s00161-014-0405-2

Placidi L., Barchiesi E., dell'Isola F., Maksimov V., Misra A., Rezaei N., Scrofani A., Timofeev D., On a hemi-variational formulation for a 2D elasto-plastic-damage strain gradient solid with granular microstructure, Mathematics in Engineering, 5(1) (2022a) 1–24. https://dx.doi.org/10.3934/mine.2023021

Placidi L., Barchiesi E., Misra A., Timofeev D., Micromechanics-based elasto-plastic–damage energy formulation for strain gradient solids with granular microstructure, Continuum Mechanics and Thermodynamics, 33(5) (2021) 2213–2241. https://doi.org/10.1007/s00161-021-01023-1

Placidi L., dell'Isola F., Kandalaft A., Luciano R., Majorana C., Misra A., A granular micromechanic-based model for ultra high performance fiber-reinforced concrete (UHP FRC), International Journal of Solids and Structures, 297 (2024) 112844. https://doi.org/10.1016/j.ijsolstr.2024.112844

Placidi L., Timofeev D., Maksimov V., Barchiesi E., Ciallella A., Misra A., dell'Isola F., Micro-mechano-morphology-informed continuum damage modeling with intrinsic 2nd gradient (pantographic) grain–grain interactions, International Journal of Solids and Structures, 254–255 (2022b) 111880. https://doi.org/10.1016/j.ijsolstr.2022.111880

Ramaglia G., Lignola G.P., Fabbrocino F., Prota A., Numerical investigation of masonry strengthened with composites, Polymers, 10(3) (2018) 334. https://doi.org/10.3390/polym10030334

Ransing R., Gethin D., Khoei A., Mosbah P., Lewis R., Powder compaction modelling via the discrete and finite element method, Materials & Design, 21(4) (2000) 263–269. https://doi.org/10.1016/S0261-3069(99)00081-3

Reccia E., Eremeyev V.A., On nonlinear rheology of masonries and granular media, International Journal of Engineering Science, 198 (2024) 104053. https://doi.org/10.1016/j.ijengsci.2024.104053

Richard P., Nicodemi M., Delannay R., Ribiere P., Bideau D., Slow relaxation and compaction of granular systems, Nature Materials, 4(2) (2005) 121–128. https://doi.org/10.1038/nmat1300

Roscoe K.H., Burland J.B., On the generalized stress-strain behaviour of wet clay, in: J. Heyman, F. Leckie (Eds.), Engineering Plasticity, Cambridge University Press, Cambridge, UK, (1968), pp. 535–609, ISBN: 978-0521052542.

Russell A.R., A compression line for soils with evolving particle and pore size distributions due to particle crushing, Géotechnique Letters, 1(1) (2011) 5–9. https://doi.org/10.1680/geolett.10.00003

Sarar B.C., Yildizdag M.E., Abali B.E., Comparison of homogenization techniques in strain gradient elasticity for determining material parameters, in: Altenbach H., Berezovski A., dell'Isola F., Porubov A. (Eds.), Sixty Shades of Generalized Continua, Advanced Structured Materials, Springer, Cham, 2023, pp. 631–644, ISBN: 978-3031261862. https://doi.org/10.1007/978-3-031-26186-2_39

Sethi G., Myers N., German R.M., An overview of dynamic compaction in powder metallurgy, International Materials Reviews, 53(4) (2008) 219–234. https://doi.org/10.1179/174328008X309690

Sinka C., Modelling powder compaction, KONA Powder and Particle Journal, 25 (2007) 4–22. https://doi.org/10.14356/kona.2007005

Stilz M., dell'Isola F., Giorgio I., Eremeyev V.A., Ganzenmüller G., Hiermaier S., Continuum models for pantographic blocks with second gradient energies which are incomplete, Mechanics Research Communications, 125 (2022) 103988. https://doi.org/10.1016/j.mechrescom.2022.103988

Suescun-Florez E., Roslyakov S., Iskander M., Baamer M., Geotechnical properties of BP-1 lunar regolith simulant, Journal of Aerospace Engineering, 28(5) (2015) 04014124. https://doi.org/10.1061/(ASCE)AS.1943-5525.0000462

Tahir S., Ariffin A., Fracture in metal powder compaction, International Journal of Solids and Structures, 43(6) (2006) 1528–1542. https://doi.org/10.1016/j.ijsolstr.2005.10.010

Timofeev D., Barchiesi E., Misra A., Placidi L., Hemi-variational continuum approach for granular solids with damage-induced anisotropy evolution, Mathematics and Mechanics of Solids, 26(5) (2021) 738–770. https://doi.org/10.1177/1081286520968149

Villard P., Chevalier B., Le Hello B., Combe G., Coupling between finite and discrete element methods for the modelling of earth structures reinforced by geosynthetic, Computers and Geotechnics, 36(5) (2009) 709–717. https://doi.org/10.1016/j.compgeo.2008.11.005

Vogler T., Lee M., Grady D., Static and dynamic compaction of ceramic powders, International Journal of Solids and Structures, 44(2) (2007) 636–658. https://doi.org/10.1016/j.ijsolstr.2006.05.001

Wiącek J., Parafiniuk P., Stasiak M., Effect of particle size ratio and contribution of particle size fractions on micromechanics of uniaxially compressed binary sphere mixtures, Granular Matter, 19 (2017) 34. https://doi.org/10.1007/s10035-017-0719-4

Wu C.Y., Hancock B., Mills A., Bentham A., Best S., Elliott J., Numerical and experimental investigation of capping mechanisms during pharmaceutical tablet compaction, Powder Technology, 181(2) (2008) 121–129. https://doi.org/10.1016/j.powtec.2006.12.017

Wu C.Y., Ruddy O., Bentham A., Hancock B., Best S., Elliott J.,

Modelling the mechanical behaviour of pharmaceutical powders during compaction, Powder Technology, 152(1–3) (2005) 107–117. https://doi.org/10.1016/j.powtec.2005.01.010

Wu M., Wang J., Zhao B., DEM modeling of one-dimensional compression of sands incorporating statistical particle fragmentation scheme, Canadian Geotechnical Journal, 59(1) (2022) 144–157. https://doi.org/10.1139/cgj-2020-0308

Wu Y., Yamamoto H., Izumi A., Experimental investigation on crushing of granular material in one-dimensional test, Periodica Polytechnica Civil Engineering, 60(1) (2016) 27–36. https://doi.org/10.3311/PPci.8028

Xu M., Song E., Cao G., Compressibility of broken rock-fine grain soil mixture, Geomechanics and Engineering, 1(2) (2009) 169–178. https://doi.org/10.12989/gae.2009.1.2.169

Yamamuro J.A., Bopp P.A., Lade P.V., One-dimensional compression of sands at high pressures, Journal of Geotechnical Engineering, 122(2) (1996) 147–154. https://doi.org/10.1061/(ASCE)0733-9410(1996)122:2(147)

Yang H., Abali B.E., Timofeev D., Müller W.H., Determination of metamaterial parameters by means of a homogenization approach based on asymptotic analysis, Continuum Mechanics and Thermodynamics, 32 (2020) 1251–1270. https://doi.org/10.1007/s00161-019-00837-4

Yildizdag M.E., Placidi L., Turco E., Modeling and numerical investigation of damage behavior in pantographic layers using a hemivariational formulation adapted for a Hencky-type discrete model, Continuum Mechanics and Thermodynamics, 35 (2023) 1481–1494. https://doi.org/10.1007/s00161-022-01154-z

Yilmaz N., Placidi L., Misra A., Fabbrocino F., A parametric study on a granular micromechanics continuum-based hemivariational approach: unraveling the emergence of critical states in granular materials, Mathematics and Mechanics of Complex Systems, 13(1) (2025) 25–54. https://doi.org/10.2140/memocs.2025.13.25

Yilmaz N., Yildizdag M.E., Fabbrocino F., Placidi L., Misra A., Emergence of critical state in granular materials using a variationally-based damage-elasto-plastic micromechanical continuum model, International Journal for Numerical and Analytical Methods in Geomechanics, 48(13) (2024) 3369–3391. https://doi.org/10.1002/nag.3795

Zhou B., Wang J., Wang H., A new probabilistic approach for predicting particle crushing in one-dimensional compression of granular soil, Soils and Foundations, 54(4) (2014) 833–844. https://doi.org/10.1016/j.sandf.2014.06.014

Authors' Short Biographies

Nurettin Yilmaz is a Graduate Assistant in the Department of Civil Engineering at Florida International University. His research focuses on the mechanical behavior of granular materials using a granular micromechanics approach (GMA) based continuum model, as well as the design of metamaterials with complex microstructures through the application of numerical methods. He is currently continuing his work in granular micromechanics and granular motif metamaterials. He received his M.S. in Civil Engineering from the University of L'Aquila in 2019. He has co-authored journal articles and presented his research at several international conferences.

Prof. Luca Placidi graduated in Physics from the University of Naples Federico II. Second degree in Engineering at the Virginia Polytechnic Institute. He took his first PhD at the Technical University of Darmstadt and his second PhD at the University of Rome La Sapienza. He was the holder of Research Fellowships from the University La Sapienza of Rome and the University of Roma Tre. He is now a Professor at the Telematic University Pegaso. He was previously at the International Telematic University Uninettuno. Bibliometrics Scopus (AU-ID: 57199322424): 122 papers, more than 5715 citations from 2131 documents, *h*-index 45. Bibliometrics ISI (X-2685-2019): 100 publications, 4590 total citations, 1786 citing articles, *h*-index 40.

Prof. Anil Misra is the Chair and Professor of the Civil and Environmental Engineering department at Florida International University. He has more than 35 years of experience in the areas of multi-scale modeling, constitutive behavior of interfaces, granular soils, and cement/asphalt concrete, as well as multi-modal material characterization using high-resolution techniques. He has pioneered the method of granular micromechanics. He has co-edited four books, guest-edited six journal special issues, and authored more than 350 papers in journals, edited books and conference proceedings. He serves as a reviewer for multiple journals and extramural funding agencies and provides consulting services to industry.